Acta Geophysica (2024) 72:2521–2553
https://doi.org/10.1007/s11600-023-01226-x

RESEARCH ARTICLE - APPLIED GEOPHYSICS

Upper-crustal structure, compositions and tectonic settings obtained from Perur–Chikmagalur 3-C seismic profile of Archean Dharwar Province, southern India

Deepak Kumar[1] · **Laxmidhar Behera**[1]

Received: 7 November 2022 / Accepted: 25 October 2023 / Published online: 6 December 2023

Abstract
We present upper-crustal *P*- and *S*-wave velocity models (V_P and V_S) of the Archean Dharwar Province in southern India using both refraction and reflection phases of the 3-C seismic data along NE-SW-oriented 200-km long Perur–Chikmagalur profile. The velocity models reveal alternate horst and graben structures at shallow depth (0.5–2.5 km) filled with weathered volcano–sedimentary rocks toward Western Dharwar Craton (WDC) having low V_P (5.20–5.58 km/s), V_S (3.20–3.32 km/s), V_P/V_S (1.63–1.68) and Poisson's ratio σ (0.20–0.25) as compared to exposed granite and gneissic rocks of increased velocity along Eastern Dharwar Craton (EDC). The steeply dipping Chitradurga Shear Zone (CSZ) imaged extends to 6–8 km depth with anomalously high V_P (6.85 km/s), V_S (3.80 km/s), V_P/V_S (1.80) and σ(0.28) comprising of deep crustal rocks impounded at shallow level. The complex suturing and oblique convergence occurred along CSZ with distinct compositions because of the shearing and transpression of EDC and WDC followed by compression and inter-wedging of the two blocks. The compositions of Neoarchean EDC are mainly felsic granites having relatively low V_P(6.25–6.30 km/s) and V_S (3.53–3.62 km/s). On the other hand, the Mesoarchean WDC is dominated by gneisses and green schists mainly corresponds to mafic and ultramafic compositions having comparatively higher V_P (6.30–6.85 km/s) and V_S (3.55–3.80 km/s) with corresponding variations of V_P/V_S (1.74–1.77), σ (0.26–0.27) for EDC and V_P/V_S (1.73–1.80), σ (0.25–0.28) for WDC. A distinct zone of detachment imaged at 3–11 km depth acts as a major unconformity having eastward-dipping low-velocity-layer (LVL) sandwiching Dharwar schist belts and Archean gneisses within the upper crust forming a complex Archean Province of southern India.

Keywords Traveltime inversion · V_P and V_S · Poisson's ratio · LVL · Composition · Dharwar Craton

Introduction

Archean rocks (~3.0–3.5 Ga) are mainly found on the surface of the Earth because of erosion and complex tectonic activity, which form stable continental craton or cratonic nuclei in different regions globally. In the southern India, the Dharwar Craton (DC) plays an important role as one of the stable continental cratons of the world, which attract the geoscientists globally to understand the complexity and evolutionary process of this craton. Nevertheless, there are several ongoing research and debates going on about the evolution and tectonic settings of this complex Archean Province of DC, but none of these theories or hypotheses proposed are satisfactory. The dominant rocks of this Archean craton are mainly of metamorphic or igneous type consisting of granites, gneisses and greenstones (GGG). Due to contemporaneous volcanic activity during Archean, there are several flows of lava eruption mainly of komatiite magmas having dyke swarms, hot spots and rift valleys predominate over DC. Besides volcanic activity, Dharwar Craton is also associated with several prominent shear zones such as CSZ and BSZ (Bababudan Shear Zone) as well as large-scale batholiths like Closepet Granite (CG) and surrounded by alternate horst and grabens with deposition of volcano–sedimentary assemblages, greywackes, mudstones and other precious mineral deposits. The Archean cratons of the world have widespread occurrence of granite–gneiss–greenstones

Edited by Dr. Seyed Yaser Moussavi Alashloo (ASSOCIATE EDITOR) / Prof. Gabriela Fernández Viejo (CO-EDITOR-IN-CHIEF).

✉ Laxmidhar Behera
laxmidhar@ngri.res.in

[1] CSIR-National Geophysical Research Institute (CSIR-NGRI), Uppal Road, Hyderabad 500007, India

(Condie 1994), and hence, the Dharwar Craton is also considered as one of the important GGG provinces of the world.

The Dharwar Craton has been extensively studied using geological (Krogstad et al. 1989; Nutman et al. 1996; Chadwick et al. 2000; Manikyamba et al. 2004, 2014; Manikyamba and Kerrich 2012; Dey 2013; Ram Mohan et al. 2013), geophysical (Kaila et al. 1979; Reddy et al. 2000; Rai et al. 2003; Sarkar et al. 2001, 2003; Rao et al. 2015a, b; Pandey et al. 2018; Behera and Kumar 2022) and geochronological (Chardon et al. 1998, 2002, 2008, 2011, 2014; Chadwick et al. 2000, 2007; Jayananda et al. 2000, 2006, 2013a, b; Bhaskar Rao et al. 2008; Kumar et al. 2012; Dey 2013) surveys with the help of several geotransects to decipher subsurface geological complexity, composition and rheology of different rock types and tectonic framework. Nevertheless, many new insights are envisaged with diverse studies conducted in this Archean Province of India. The main aim of our study is to decipher detailed subsurface geological structures from the V_P and V_S models along with obtaining new insights of upper-crustal rock compositions by the analysis of the 3-C seismic data acquired along Perur–Chikmagalur profile in DC of southern India (Fig. 1a). The modeling and inversion of 3-C seismic data have an added value over the conventional analysis of single-component (vertical) *P*-wave data acquired along the same profile by Rao et al. (2015a, b). We have used both the *P*- and *S*-waves to obtain additional information like V_P, V_S, V_P/V_S, Poisson's ratio (σ), and presence of fluids within the rock formations, understanding the rock compositions and lithology of the subsurface rock types of the upper crust to assess its mineral assemblages from the suitable analysis and modeling/inversion of 3-C seismic data. This study mainly focuses on comprehensive understanding of the tectonic settings by developing a plausible tectonic and geodynamic model with an emphasis on the precious mineral assemblages (gold, copper, diamond and PGE mineralization) and their deposits in the shallow upper crust of this greenstone province of DC due to contemporaneous Meso- and Neoarchean mafic–ultramafic magmatism. The results of this study will definitely help exploration of economic mineral deposits in the shear zones, mafic dykes and other shallow high-resolution upper-crustal geological structures delineated in the Archean Dharwar Province having proven gold deposits in greenstone complexes of Kolar, Ramagiri and Hutti gold mines along the eastern margin of CSZ, copper–nickel (Cu–Ni) mineralization in the Sargur and Chitradurga Groups as well as several diamondiferous kimberlite–lamproite mineralization in this region (Devaraju et al. 2009).

The main objective of this study is to present new insights into the causative factors controlling the development of large batholiths like CG, imaging of major faults/shear zones akin to CSZ and BSZ in this complex Archean Dharwar Craton by using 3-C seismic data. Also, the analysis of 3-C seismic data acquired in the Dharwar Craton could able to (1) decipher the upper-crustal velocity models (V_P and V_S), (2) compute bulk physical properties of the subsurface rock types based on the variations of V_P/V_S and σ with suitable assessment of the presence of traveltime skips observed in both *P*- and *S*-wave data, (3) obtain a tectonic model describing different processes responsible for the formation of the CSZ acting as a major suture zone and (4) delineate subsurface extension of large-scale intrusions like CG, presence and extension of BSZ, horst and grabens as well as numerous other geological structures like faults/thrusts, folds, unconformities/detachments prevalent in the DC of southern India.

Geology and tectonic framework

The Dharwar Craton is exposed over an area of about 250,000 km^2 shown between 12° to 15° N and 74° to 80° E with large exposures of granites, gneisses, schists and greenstones forming a geologically complex terrain (Fig. 1a). The greenstones are mainly composed of voluminous basalts, sediment-impoverished with clastics and ripple-bedded quartzites, shelf/shallow water sediments like dolomites and limestones. The greenstone belts of EDC are gold rich (Hutti and Kolar gold mines), in contrast to those of WDC. Both volcanics and sediments forming the supracrustal rocks were deposited at shallow levels over the peninsular gneissic complex (> 3.0 Ga) of DC. These volcanic rocks were metamorphosed to greenschists, amphibolites and basic granulites, while the corresponding sediments have been recrystallized to form quartzites, metapelites and crystalline marbles (Sharma 2009). Toward east of this region, there is presence of numerous shear zones bounded by major schist belts. The Dharwar Craton is considered as one of the Archean GGG terrain of the world with ubiquitous presence of tonalite–trondhjemite–granodiorite (TTG) gneisses. The two prominent blocks of the DC are called Neoarchean EDC and Mesoarchean WDC, which are divided by the highly sheared and mylonitized CSZ. The basement of WDC primarily comprises TTG gneisses (3.4–2.9 Ga) over which greenstones (e.g., volcano–sedimentary rocks) are deposited during 2.9–2.6 Ga. On the other hand, the basement of EDC is mainly consists of granitic plutons (2.5 Ga) of CG and equivalents, which are intruded through the TTG gneisses forming narrow elongated greenstone belts (Chadwick et al. 2007; Rao et al. 2015a). The TTG suite is opined to be produced because of partial melting of mafic crust and final phase differentiate of mantle materials leading to both vertical and horizontal crustal growth (Sharma 2009).

Besides this, ubiquitous presence of the widespread komatiite magmas in association with fine clastics, basal-conglomerates and ripple-bedded quartzites are prevalent

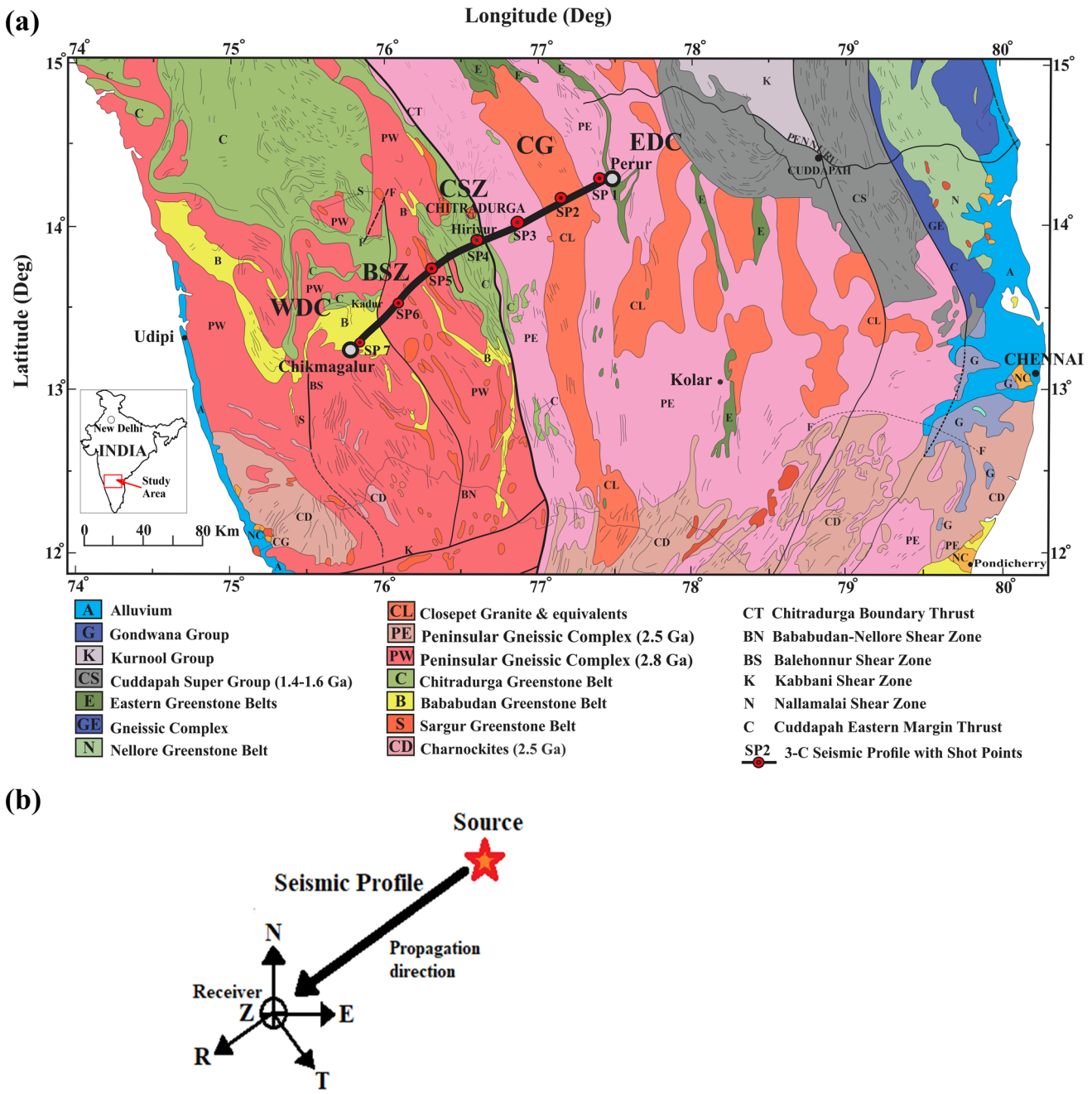

Fig. 1 **a** Geological map of the Dharwar Craton (DC) with NE-SW trending 200-km-long Perur–Chikmagalur 3-C seismic profile shown for seven 3-C shot points (SP1 to SP7) acquired in the EDC and WDC part of it. The Closepet Granite (CG) acts as a major batholith of the Dharwar Craton with the presence of major shear zones like Chitradurga Shear Zone (CSZ) and Bababudan Shear Zone (BSZ). The important faults and shear zones, as well as different rock types exposed on the surface, are indicated with respective color legends. The study area is shown on the India map as inset (Modified after GSI, ISRO 1994). **b** The 3-C seismic data acquired for each SP along the profile are in vertical (*Z*), north (N) and east (E) components (Cartesian co-ordinates), which are rotated with respect to the profile direction as shown for each receiver station forming corresponding vertical (*Z*), radial (*R*) and transverse (*T*) components so that the maximum energy propagation should be observed along the seismic profile (**a**), which coincides with the radial (*R*) component. These radial component seismic data for both *P*- and *S*-waves are used for further analysis to obtain corresponding *P*- and *S*-velocity models

in most of the regions of WDC forming the greenstone or schist belts. The peninsular gneisses with association of tonalitic gneisses and older metavolcanic metasedimentary rocks as enclaves are classified under Sargur Group of the DC. Hence, the basement is mainly formed by peninsular gneisses over which the supracrustals were laid with older

Table 1 Simplified stratigraphy of Archean Dharwar Craton (Modified after Swami Nath and Ramakrishnan 1981; Ramakrishnan and Vaidyanadhan 2010)

Age (Ga)	Western Dharwar Craton (WDC)	Eastern Dharwar Craton (EDC)
2.5-2.6	Younger Granite (Chitradurga, Arsikere) Charnockite	Younger granite / gneiss (Closepet and equivalents) Charnockite
	Chitradurga Group	Kolar Group
2.6-2.8	Bababudan Group (Dharwar Supergroup)	Yashwantnagar Formation (Dharwar Supergroup)
	----------Unconformity----------	----------Unconformity---------
~3.0	Peninsular Gneiss	Enclaves of older Gneiss
3.1-3.3	Sargur Group	
3.3-3.4	Gorur Gneiss	Putative Basement

tonalitic gneisses (Dharwar Group) and rocks of Sargur Group (Swami Nath and Ramakrishnan 1981; Naqvi and Rogers 1987; Sharma 2009). Table 1 shows the generalized stratigraphy of the Dharwar Craton with major classifications of EDC and WDC blocks. The regional unconformity demarcates large-scale denudation led to the cessation of the Sargur orogeny. The similar well-known unconformities of the world are identified with the presence of quartz–pebble conglomerates, which are locally uraniferous and may sporadically contain copper and gold. The abundance of younger granites mainly supplied the necessary advective heat required for the low-pressure metamorphism of EDC. Due to this, many mafic and ultramafic (komatiite) complexes with intense magmatism were reported from Sargur-Hassan of WDC and Kolar gold field region of EDC (Fig. 1a). Also, the oldest rocks more than 3.4–3.3 Ga are preserved in the Sargur Group mainly associated with numerous slivers having mafic–ultramafic rocks generally occurred in the supracrustal or greenstone belts of WDC.

There are different models that exist to explain the tectonic settings of the Dharwar Craton, which are always been debated. However, non-uniformitarian hypothesis of sagduction (i.e., passive sinking of volcanic and sedimentary basins into basement gneisses without crustal thinning) as argued by Chardon et al. (1996, 1998) and Choukroune et al. (1997) controls the tectonic evolution of the DC. On the other hand, uniformitarians strongly support the hypothesis of continent–continent collision followed by crustal accretion as the main cause of the evolution of the DC (Naqvi 1985; Radhakrishna and Naqvi 1986; Chadwick et al. 1997, 2000). In WDC, the geodynamic perspective of komatiite magma generation along with sub-contemporaneous mafic to felsic volcanic eruption is still a matter of argument, as whether they are related to mantle plume (Ohtani et al. 1989; Arndt et al. 1997; Kerrich and Xie 2002; Arndt 2003), an oceanic plateau originated from mantle plume (Kerr et al. 1996; Polat and Kerrich 2000), a combined mantle plume-island arc environment (Puchtel et al. 1999) or a subduction zone (Perman et al. 1997, 2001). On the other hand, the felsic volcanism of EDC is coeval with and genetically linked to widespread juvenile calc-alkaline magmatism and crustal reworking (Chadwick et al. 2007; Chardon et al.

2008, 2011). The two episodes of volcanism and associated plutonism relate to two crustal accretion events contributing to continental growth of EDC and reworking of the eastern fringe of WDC (Jayananda et al. 2006, 2013a; Chardon et al. 2008, 2011). Hence, a combined model taking into account plume-arc setting has been proposed to explain the Neoarchean accretion and tectonic evolution of EDC (Harish Kumar et al. 2003).

Data

3-C data acquisition

The 3-C seismic data were acquired in the Dharwar Craton covering EDC and WDC blocks (Fig. 1a). These data help to decipher compositions of different rock types and comprehend the geology/tectonic framework of this important GGG terrain of the world. CSIR-NGRI (CSS Group) has acquired the 3-C seismic data by deploying independent Taurus Seismographs (Nanometrics Inc., Canada) along the Perur–Chikmagalur profile of DC in which single (vertical) component *P*-wave data were also acquired (Rao et al. 2015a, b) using cable-based line telemetry system. The profile mainly covers important shear zones like CSZ, BSZ and other several structural features like horst and grabens, numerous faults and folds, large batholiths like CG, respectively, making this region geologically complex (Fig. 1a). The dense 3-C seismic data having seven shots are acquired with ~ 40-km SP intervals and 400 m geophone intervals. The data recording was made in continuous mode with the help of 4.5 Hz geophones (3-C) having sampling of data at 4 ms. The acquisition parameters of 3-C data are shown in Table 2. Each SP gather is obtained by merging traces from shots taken for different spreads in a sequence by shooting multiple times to acquire data for each spread (which moves along the profile for different SP coverage). Shots for each spread coverage are taken in a particular SP location area by making pattern of holes, filled with required quantity of explosives (Table 2) and blasted to generate seismic energy. The number of shot holes and the corresponding charge size vary for each pattern coverage, which increases with increase of offset from source to the receivers for a particular spread. The spread moves after required number of shots are taken corresponding to each SP along the profile. For each spread, a maximum 45 standalone Taurus Seismographs with same number of 3-C geophones are used for recording of 3-C seismic data (Table 2). The data gap (Figs. 2 and 3) arises due to logistic problems that occurred in the field and shots with that particular spread could not be activated for which the missing channels of the spread were padded to make the uniform number of traces for each SP, but active data channels vary for each SP (Table 2).

Data analysis and pre-processing of 3-C seismic data

The analysis of 3-C seismic data provides important information on the geologically plausible structures and composition of rocks. The 3-C geophone configuration used is mainly Cartesian having three orthogonal elements oriented in axial, transverse and vertical directions. The two horizontal components radial (*R*) and transverse (*T*) are formed by the axial and transverse elements in which the radial component is oriented along the seismic profile and the transverse component oriented perpendicular to the profile. The vertical component (*Z*) points orthogonal to other two components (e.g., *R* and *T*) and points vertically downward (Fig. 1b). In our case the profile direction is mainly

Table 2 3-C seismic data acquisition parameters

Data acquisition system	: 45 no. of Standalone Taurus 3-C Seismographs (Nanometrics, Canada)
Shot point (SP) interval	: 35–40 km
Type of source used	: Explosives (Class II Emulsion Seismic Plus) with detonators
Shot hole depth	: 25–28 m (Group/Pattern of holes used for each SP)
Numbers of wide-angle 3-C SPs	: 7
Total no. of traces per SP	: 567
Charge size used for each SP	: 75–1850 kg explosives depending upon maximum offset of the spread
Spread length	: 18 km
No. of spreads	: 13 (Spreads 1 to 12 have 45 traces each and spread 13 has 27 traces)
Geophones	: 3-C, 4.5 Hz
Geophone interval	: 400 m
No. of 3-C Geophones in a spread	: 45 (Spread no. 13 has 27 Geophones)
Type of data	: NMX, SEED, Mini-SEED and SEG-Y (Continuous)
Sampling interval	: 4 ms
Record length	: 60 s (downloaded)

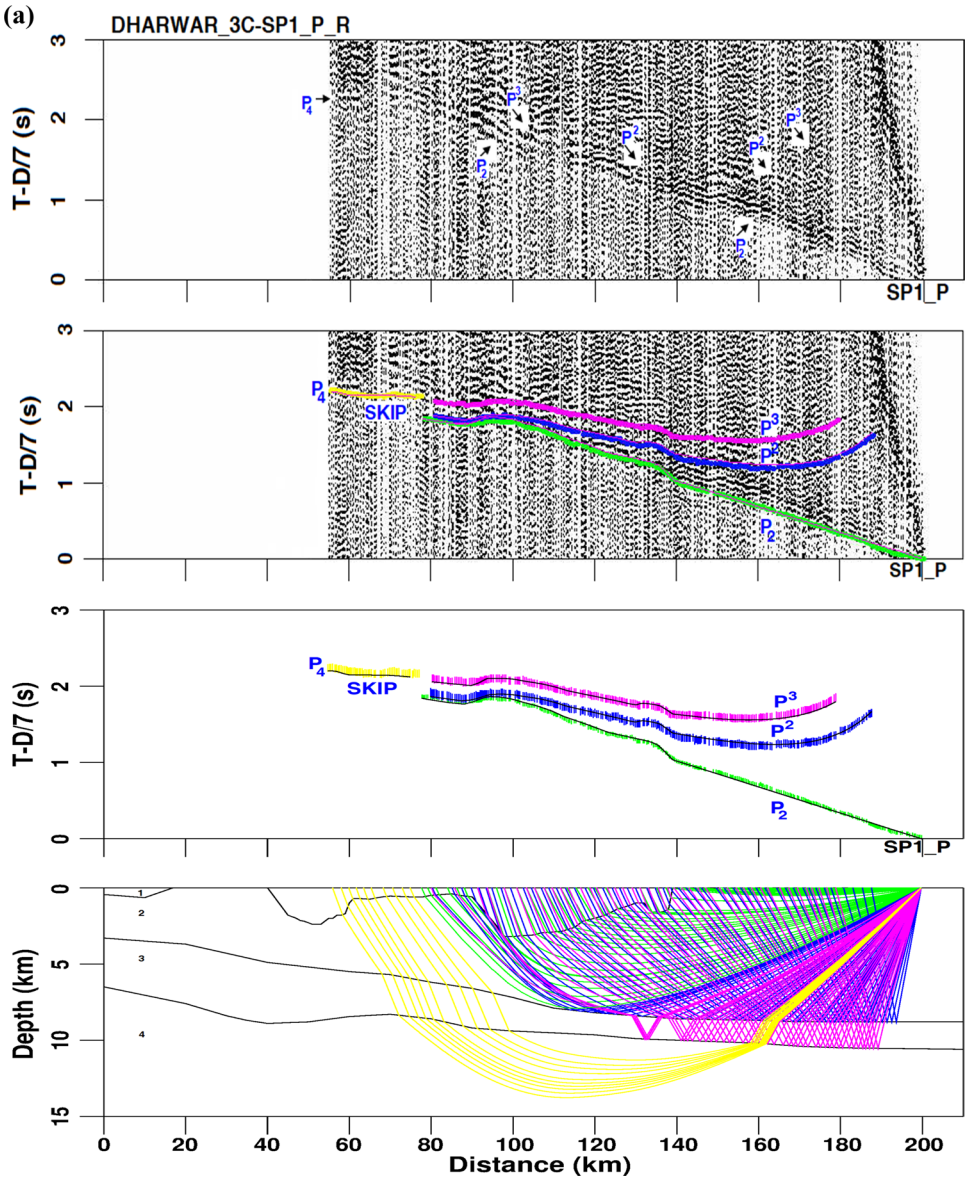

Fig. 2 The observed seismic data (unpicked and picked shown for top two panels) for the radial component *P*-wave shot gathers with corresponding synthetic responses computed superimposed on the picked data for the model derived using ray-trace inversion shown for **a** SP1, **b** SP5 as example (other shot gathers SP2 to SP7 are shown as Supplementary Fig. S1) along the Perur–Chikmagalur 3-C seismic profile. The top panel for each figure (**a** to **b**) shows the processed shot gathers (observed data) without any data pick; the panel below it shows the corresponding data picked (first-arrival refraction P_1, P_2, P_4 and reflection P^2, P^3 phases shown with corresponding colored dots) for each SP, which are used for traveltime inversion. Middle panel of each figure (**a** to **b**) shows the traveltime fit of the observed data (colored vertical bars) with corresponding synthetic responses (solid black line) computed for each layer. Bottom panel of each figure (**a** to **b**) shows the corresponding ray-trace inversion through the different layers (1 to 4) of the final *P*-wave velocity model derived. The data are displayed in the time scale with 7.0 km/s reduction velocity

ENE-WSW, hence the ZNE component of the 3-C seismic data recorded for each geophone is rotated to obtain the corresponding ZRT component (Fig. 1). After component rotation (Fig. 1b), the *R* component geophones point toward the profile direction, hence receives maximum source energy than the *Z* and *T* component geophones (Guevara and Stewart 1998). The individual component gathers of different SPs are prepared from the traces of each 3-C geophones after component rotation. This is followed by pre-processing of shot gathers (SP1-7) with application of field geometry, muting and editing of noisy/dead traces, spherical divergence/geometrical spreading correction, application of field statics due to weathering and topographic relief or elevations (i.e., shot and receiver statics, datum statics as explained in Appendix 1), spiking deconvolution and band-pass filtering (Table 3) for further data analysis and modeling. The main purpose of spiking deconvolution is to improve the temporal resolution of seismic data by compressing the basic seismic wavelet into a spike so that the band-width of the signal will be increased and suppress the reverberations. Since spiking deconvolution broadens the spectrum of seismic data, the traces contain more high-frequency energy after deconvolution. The parameters that control the spiking deconvolution are operator length (OL), prediction delay/lag (PL) and percent prewhitening (PPW), which are obtained after series of tests for getting the optimum values as mentioned in Table 3 used for pre-processing of seismic data (Yilmaz 2001). Because of spiking deconvolution, both high-frequency noise and signals are also boosted; hence, a filtering with suitable band-pass filter (Table 3) is used after the deconvolution to bring back the data to a common root-mean-square (RMS) level for further data analysis as shown

Fig. 2 (continued)

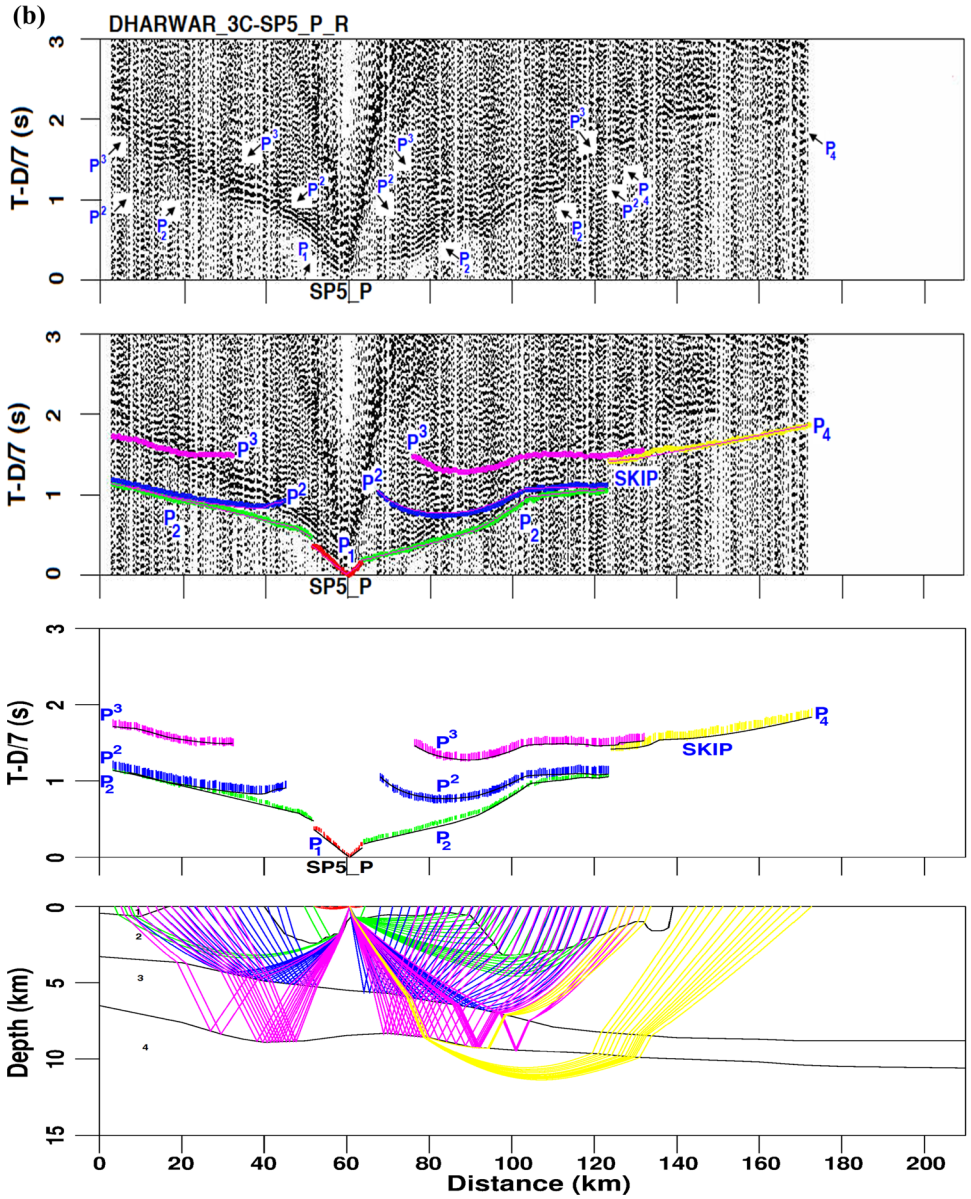

in individual shot gathers (Figs. 2, 3, S1 and S2). Since R component geophone data directs along the profile direction and receives maximum energy, these component data have been used for modeling and inversion (Zelt and Smith 1992; Zelt 1999) of *P*- and *S*-wave phases for each SP (Figs. 2, 3, S1 and S2). The most important aspects of deriving V_P and V_S models are accurate phase identification and corresponding picking of the refraction and reflection seismic data.

We have adopted the interactive software zplot of Zelt (1999) for phase identification and picking of pre-processed *P*- and *S*-wave data for each SP gather (Figs. 2, 3, S1 and S2). Since the *S*/N ratio (SNR) for radial component data is excellent, we have used these data of refraction and reflection phases (SP1 to SP7) for inversion to obtain V_P and V_S models of DC (Fig. 1). While phase identification and picking of *P*- and *S*-wave phases, we have taken utmost care to assign the picking uncertainties of each phase. The accuracy of the phases picked provides the real assessment of the errors present in the data. Hence, the picking uncertainties assigned for each phase are mainly offset-dependent and accordingly the uncertainty values for refraction and reflection phases are assigned with corresponding visual check and correlations of different arrivals along the profile (Zelt and Smith 1992; Behera et al. 2002; Behera et al. 2004; Fernandez-Viejo et al. 2005; Malinowski et al. 2005; Rumpfhuber and Keller 2009; Behera and Kumar 2022).

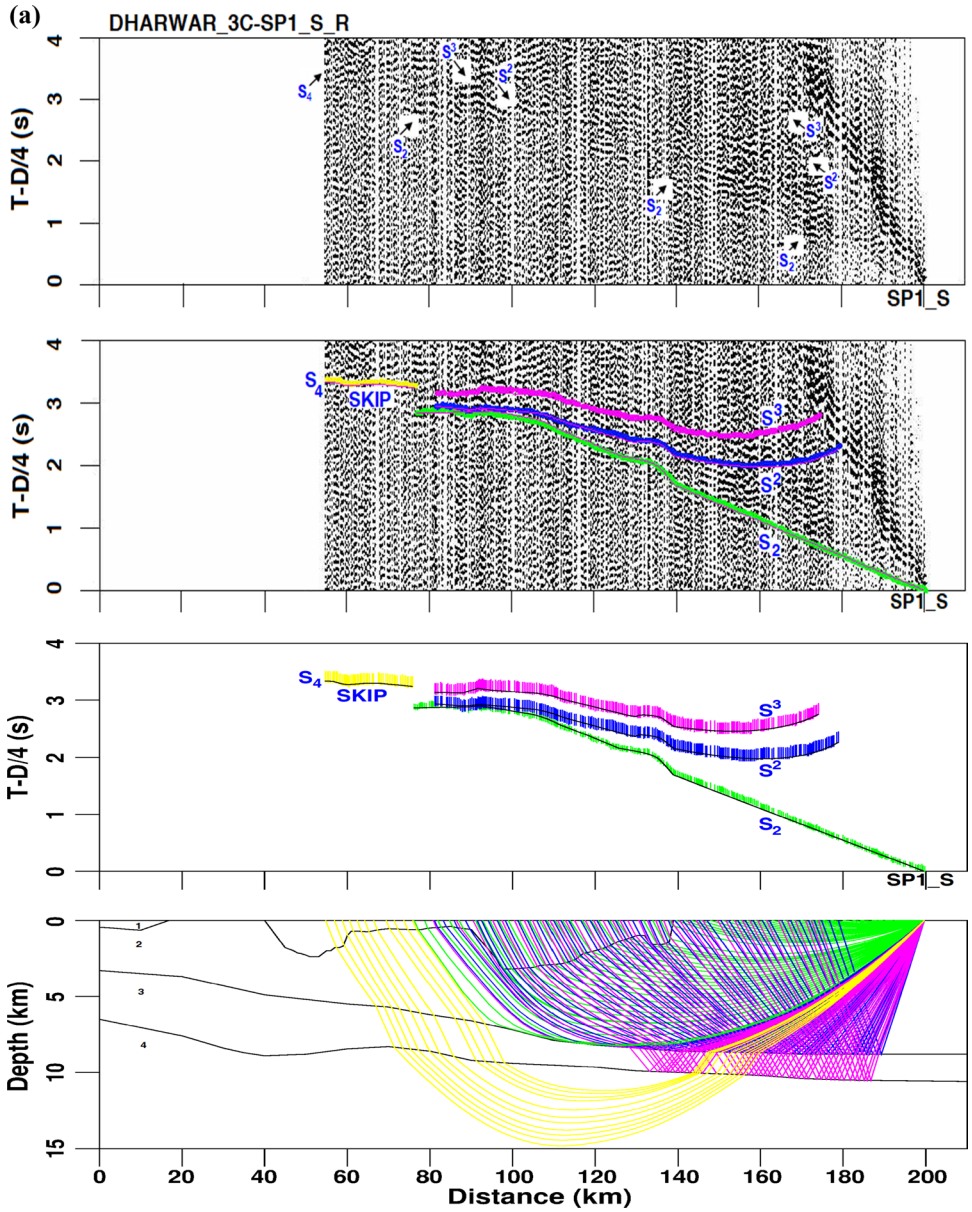

Fig. 3 The corresponding *S*-wave radial component observed seismic data without and with picks (top two panels), traveltime fit (middle panel) and ray-trace inversion (bottom panel) through the different layers of the final *S*-wave velocity model derived shown for SP1 and SP5 (**a** to **b**) as example (other shot gathers SP2 to SP7 are shown as Supplementary Fig. S2) along the same 3-C seismic profile. The data are displayed in the time scale with 4.0 km/s reduction velocity along with the first-arrival refraction S_1, S_2, S_4 and reflection S^2, S^3 phases picked for inversion are shown corresponding to the layer numbers 1 to 4 indicated within the model

The traveltimes of both *P*- and *S*-wave phases are picked for all the traces of each SP gathers along the profile (Fig. 1a), which is not obvious due to the complexity of the terrain. The picking uncertainties of ± 25 ms to ± 50 ms for direct and refracted *P*-wave arrivals (P_1, P_2,P_4) and ±50 ms for corresponding reflection phases (P^2, P^3) are assigned with proper phase classifications. The corresponding uncertainties of ± 50 ms to ± 100 ms for *S*-wave direct and refracted phases (S_1, S_2, S_4) and ±100 ms for reflection phases (S^2, S^3) are also assigned in the similar way (Table 4). The other requirement of assigning uncertainties to the traveltime data picked for ray-trace inversion is to circumvent over- or under-fitting of the observed data (Zelt 1999).

Methodology

1-D and pseudo-2-D modeling

The starting V_P and V_S models are developed from 1-D velocity–depth functions computed with the help of damped-least-square (DLS) traveltime inversion of *P*- and *S*-wave data in a layer-stripping approach (Zelt and Smith 1992; Behera et al. 2004; Behera and Sen 2014). The *P*- and *S*-wave observed traveltime data of all SPs acquired in the 3-C profile are used for inversion (Figs. 2, 3, S1 and S2). The traveltime picks (refractions and reflections) of all SPs along the profile are displayed as bars (Fig. 4) with the corresponding

Fig. 3 (continued)

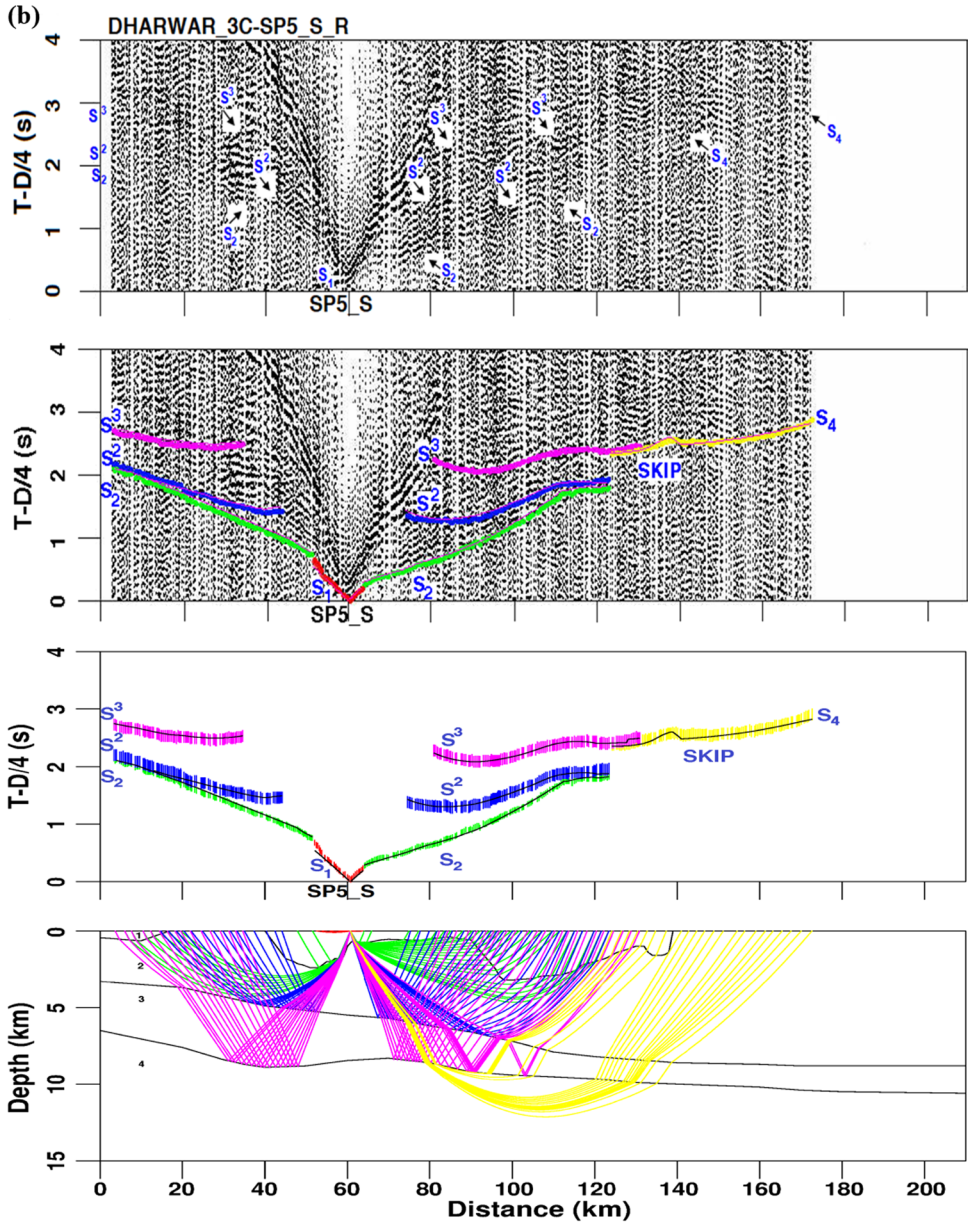

Table 3 Pre-processing of 3-C seismic data

3-C seismic data download (SEG-Y format) from Taurus Seismographs
Format verification and conversion
3-C data rotation from Cartesian ZNE to ZRT components
Sorting of traces for each individual component (*Z*, *R* and *T*)
Merging of each component traces (*Z*, *R* and *T*) to prepare individual SP gathers
Application of field geometry for individual SP gathers
Muting and Editing of Noisy/Dead Traces
Spherical divergence/Geometrical spreading correction with T^2V^1 exponential gain function
Application of field statics for weathering and elevation corrections (i.e., shot and receiver statics, datum statics)
Spiking deconvolution (OL = 0.60 s, PL = 0.08 s, PPW = 0.1%)
Band-pass filtering (3-8-24-60 Hz)

Table 4 *P*- and *S*-wave traveltime inversion results

	Phase identification	Total no. of picks	Average picking uncertainty (ms)	RMS traveltime residual (s)	Normalized χ^2	No. of rays traced through the model
All *P*	P_1, P_2, P^2, P^3,P_4	5013	40	0.046	1.087	4778
P_1	1	156	25	0.029	1.127	155
P_2	2	1440	25	0.023	1.115	1294
P^2	3	1290	50	0.054	0.950	1279
P^3	5	1381	50	0.047	1.066	1339
P_4	4	746	50	0.056	0.884	711
All *S*	S_1, S_2, S^2, S^3,S_4	4758	80	0.089	1.108	4566
S_1	1	152	50	0.058	1.256	124
S_2	2	1461	50	0.056	0.912	1391
S^2	3	1170	100	0.108	0.807	1145
S^3	5	1246	100	0.094	1.105	1212
S_4	4	729	100	0.112	0.970	694

uncertainties assigned for each phase (*P*- and *S*-waves) picked (Table 4). The corresponding computed responses of 1-D velocity models derived are superimposed on the observed data picked (*P*- and *S*-wave) to assess the nature of traveltime fit (Fig. 4). The 1-D velocity functions show average apparent velocities of 5.2 km/s, 6.2 km/s and 6.5 km/s (related to volcano–sedimentary layer, basement and upper-crustal rocks, respectively) relate to the different traveltime segments with increasing offsets of the *P*-wave first-arrival traveltime data (Fig. 4a). The skips from SP1 to SP7 of the observed data signify the existence of a low-velocity-layer (LVL) located beneath the high-velocity-layer (HVL) as basement (6.2 km/s) corresponding to the second layer. The corresponding thickness and extension of the LVL (apparent velocity 5.8 km/s) are constrained from the nature and extent of skip or delay in traveltime present in individual SP gather (Figs. 2, S1 and 4a), which varies from 0.3 s at SP1 to 0.8 s toward SP7 along the profile with gradual thinning toward northeast (Fig. 1a). The apparent V_P (5.8 km/s) of LVL is obtained by series of tests with rigorous damped-least-square 1-D inversion using layer-stripping approach of first-arrival traveltimes with skip phenomena (Zelt and Smith 1992; Sain and Kaila 1994; Behera et al. 2002, 2004). The first step of the damped-least-square 1-D inversion is the analytic calculation of partial derivatives of traveltime with respect to the model velocities and the vertical position of the corresponding depth node. These partial derivatives are calculated and may correspond to any arrival (refraction or reflection) identified in the observed seismic traveltime data. The second step is to interpolate the traveltimes and partial derivatives between the source and receiver locations followed by suitable damping factor to converge the number of iterations and reduce the RMS traveltime residuals between the observed and computed data so as to obtain chi-square $\left(\chi^2\right)$ close to 1.0. The third step is to update the model parameters selected by adjusting both velocity and boundary nodes simultaneously to continue for the next run of the 1-D inversion if the χ^2 value obtained is more than 1.0 or RMS residuals obtained are not within the permissible limit set a priori. This process is continued in a layer-stripping manner to obtain velocity and depth of each layer during the damped-least-square 1-D inversion.

The average apparent *P*-wave velocities of first and second layer are 5.2 km/s and 6.2 km/s overlying the LVL and 6.5 km/s for the fourth layer placed below the LVL obtained from the damped-least-square 1-D first-arrival *P*-wave traveltime inversions from all the SPs along the profile (Fig. 4a). Hence, the velocity of the LVL should be less than 6.2 km/s. To fit the traveltime data using the above inversion method for each SP, the velocity of the LVL was varied from 5.2 to 6.2 km/s at 0.2 km/s interval. The optimum fit has occurred for the whole data with velocity for the LVL constrained as 5.8 km/s by varying the thickness of it depending upon the amount of skip observed in both forward (positive offset) and reversed (negative offset) refraction data for different SPs (Fig. 4a). The thickness of the LVL is constrained from the amount of skips noticed for each SP and inversion of reflection phases corresponding to top and bottom of the LVL. The layer (6.5 km/s) below the LVL is stretched down to maximum 15 km depth. Similarly, the 1-D velocity functions of *S*-wave are obtained using the same inversion for *S*-wave first-arrival refraction and reflection traveltime picks (Figs. 3, S2), which show velocities of 3.25 km/s, 3.60 km/s and 3.85 km/s for traveltime segments at different offsets (Fig. 4b). The thickness and apparent velocity of the LVL (Fig. 4b) are constrained from the traveltime skip phenomena in the same layer-stripping manner by varying the *S*-wave apparent velocity of the LVL from 3.35 to 3.65 km/s at 0.1 km/s to fit the corresponding traveltimes (refraction and reflection) as used for the *P*-wave

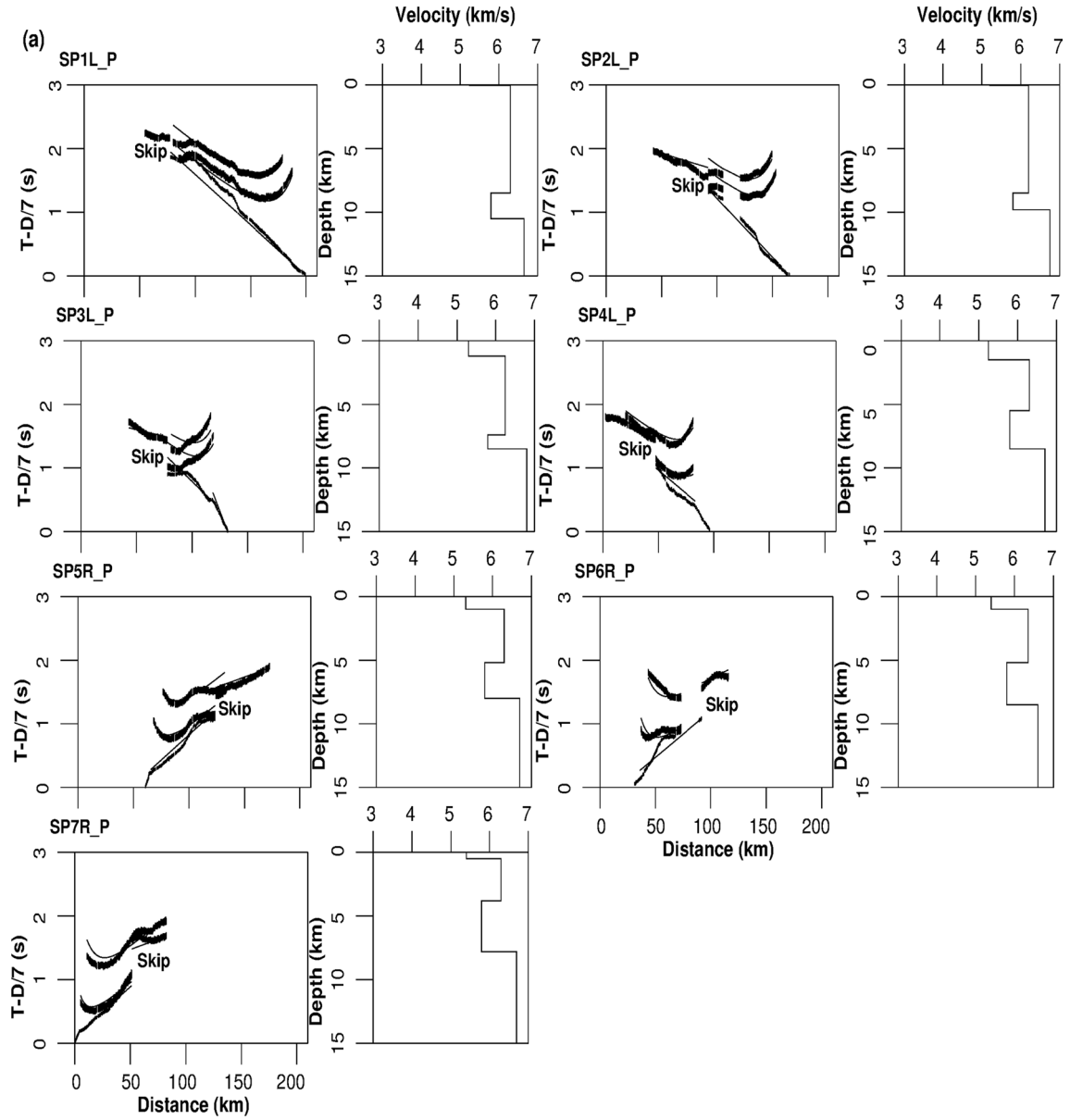

Fig. 4 **a** 1-D velocity–depth functions (right panel) obtained after damped-least-square inversion of the observed *P*-wave first-arrival traveltime data (vertical bars) shown for SP1 to SP7 with the corresponding traveltime fit (solid lines) plotted in time scale of 7.0 km/s reduction velocity (left panel) for each SP. The traveltime skips are prominent in the observed data indicating the presence of LVL and its magnitude gradually increases from SP1 to SP7 along the profile. **b** The corresponding 1-D velocity–depth functions (right panel) obtained after damped-least-square inversion of the *S*-wave picks (shown as vertical bars) for SP1 to SP7 with traveltime fit (solid lines) plotted in time-scale of 4.0 km/s reduction velocity (left panel) for each SP. The traveltime skips are also prominent, and its magnitude varies similar to *P*-wave data

data mentioned above (Zelt and Smith 1992; Sain and Kaila 1994; Behera et al. 2002, 2004).

The computed responses and the corresponding traveltime fit of *P*- and *S*-wave picks for all the SPs (Fig. 4) indicate that the 2-D traveltime inversion is necessary for the optimum fit of traveltime data along the profile. The computed 1-D functions of V_P and V_S (Fig. 4a, b) are then smoothly joined to derive the corresponding pseudo-2-D velocity models independently (Fig. 5a, b). These pseudo-2-D *P*- and *S*-wave velocity models developed (Fig. 5a, b) act as input for 2-D ray-trace inversion (Zelt and Smith 1992; Zelt 1999) of 3-C seismic data (*P*- and *S*-wave

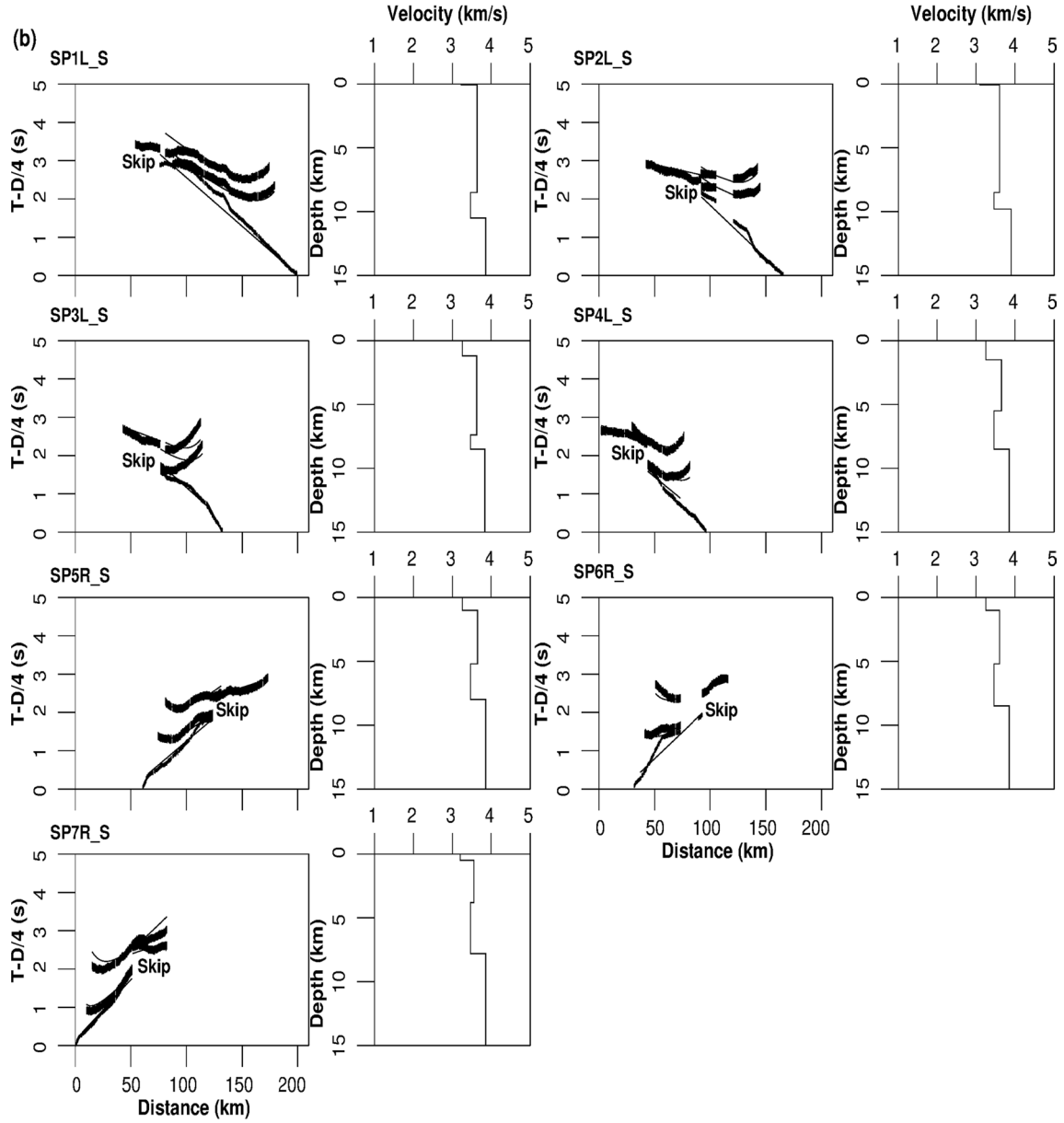

Fig. 4 (continued)

refraction and reflection phases) to derive the respective *P*- and *S*-wave upper-crustal velocity models of the Dharwar Craton without biasing inversion results.

2-D ray-trace modeling and inversion

The 2-D ray-trace modeling and inversion (rayinvr) technique is used for inverting seismic refraction and reflection traveltime data (*P*- and *S*-waves) to obtain the final V_P and V_S models, respectively (Zelt and Smith 1992). The ray-trace technique and model parameterization are suitably adjusted for the inversion algorithm by employing a forward step parameter. The ray-trace inversion algorithm is appropriate for large number of shots with their corresponding traveltime data in which forward modeling plays an important role, despite the nature of source-receiver orientation or quality of seismic data. In this approach the forward step is analogous to forward modeling of data using trial-and-error method (Červený et al. 1977; Spence 1984; Huang et al. 1986; Firbas 1987; Gajewski and Prodhel 1987; Franco 2011; Lutter et al. 1990; Zelt and Smith 1992; Behera et al. 2002, 2004, 2021; Behera 2011a, b; Behera and Sen 2014; Talukdar and Behera 2018). The ray-trace inversion method is suited to a best possible solution obtained using eikonal equations joined together with take-off angles of the rays traced through the model (Zelt and Smith 1992). Besides this, a boundary

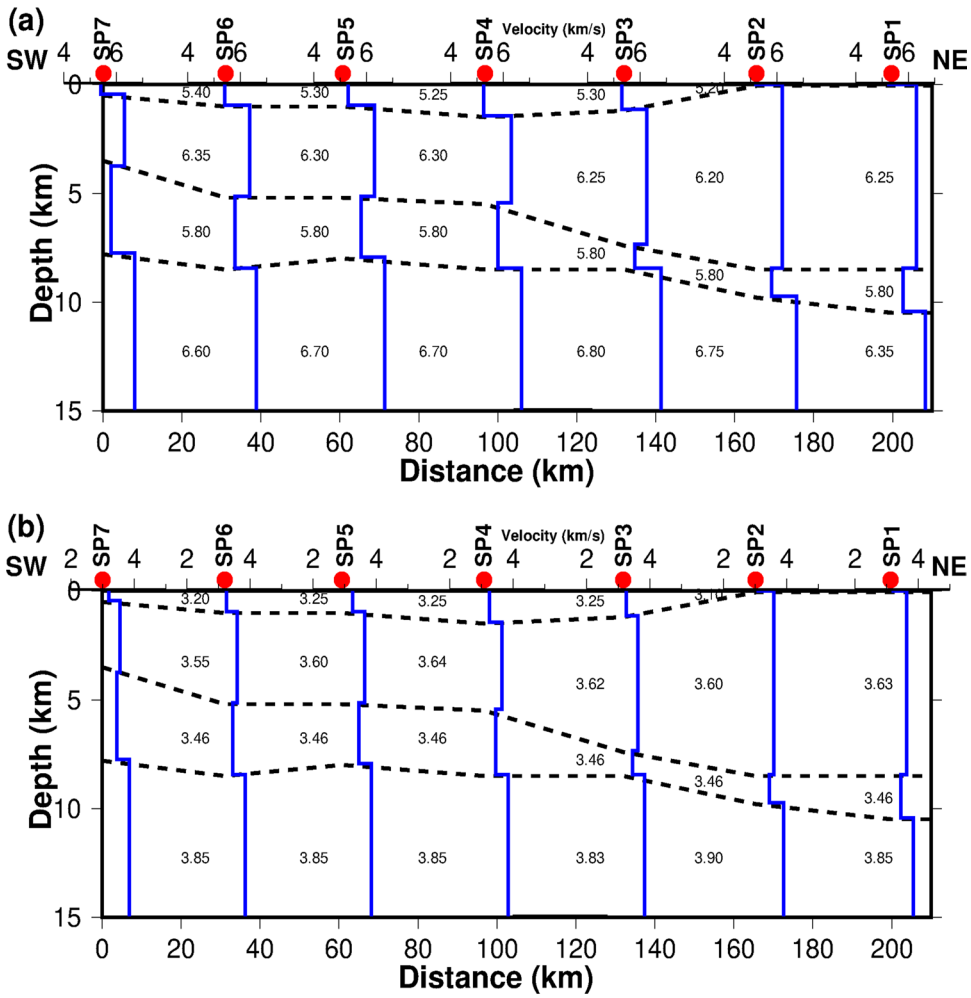

Fig. 5 **a** Pseudo-2-D *P*-wave velocity model derived by smoothly joining (dashed lines) the 1-D velocity–depth functions (solid lines) obtained (Fig. 4a) for different SPs along the profile. **b** The corresponding pseudo-2-D S-wave velocity model derived along the same profile by smoothly joining (dashed lines) the 1-D velocity–depth functions (solid lines) obtained (Fig. 4b) for different SP's along the same profile. The velocity scale for each 1-D velocity–depth function is shown on the top with corresponding *P*-wave velocity values range from 4 to 7 km/s and the *S*-wave velocities range from 2 to 5 km/s with small indents at every 1 km/s along with their apparent velocity values labeled for each layer. The individual SPs are indicated as red dots with label

simulation is also employed using smooth layering concept in the ray-trace algorithm to reduce the instability associated with blocky parameterization of the model. The analytic calculations of traveltime partial derivatives at each node of the velocity and boundary depths are also obtained using the model parameterization approach. The computation of partial derivatives for ray-trace inversion also corresponds to any type of observed traveltime data.

The interpolations are made across ray-endpoints of respective geophone positions to circumvent two-point ray-tracing (Zelt and Smith 1992). During the process of parameter update, proper alteration of nodes corresponding to velocity and boundary are made using the damped-least-square inversion (Zelt and Ellis 1988; Zelt and Smith 1992; Iannaccone et al. 1998; Zelt 1999; Behera et al. 2002, 2004, 2021; Behera 2011a, b; Behera and Sen 2014; Talukdar and Behera 2018). Both residual-vector and partial-derivative matrix of the traveltime data are computed during ray-trace iterative inversion through the model. The partial-derivative matrices are computed analytically. Hence, additional rays are not traced during the numerical approximation while computing the partial-derivatives by differencing (Zelt and Smith 1992). The parameter adjustment vector is solved after initial ray-tracing and applied to the current model followed by iterative velocity model update. This process is continued until the optimum traveltime data fit is achieved with predefined stopping condition (Spence et al. 1985; Zelt and Smith 1992).

The parameter selections are made while inversion followed by number of tests with series of values corresponding to the initial damping factor of 100 and gradually reduced during iterations. The series of different damping factors (e.g., 100, 50, 10, 5, 2, and 1) were tested, which indicates that the χ^2 misfit of the inversion should fall gradually from a very large value (of the order 30.0) to very close of 1.0 for the starting velocity model chosen. The final *P*- and *S*-wave ray-trace inversion models are derived (Figs. 6 and 8) with damping factor of 1, which provides the minimum RMS traveltime residuals of 0.046 s for *P*-wave phases and 0.089 s for S-wave phases with corresponding χ^2 misfit of 1.087 and 1.108, respectively (Table 4). The initial value of the damping factor was chosen 100 by trial and error so that the

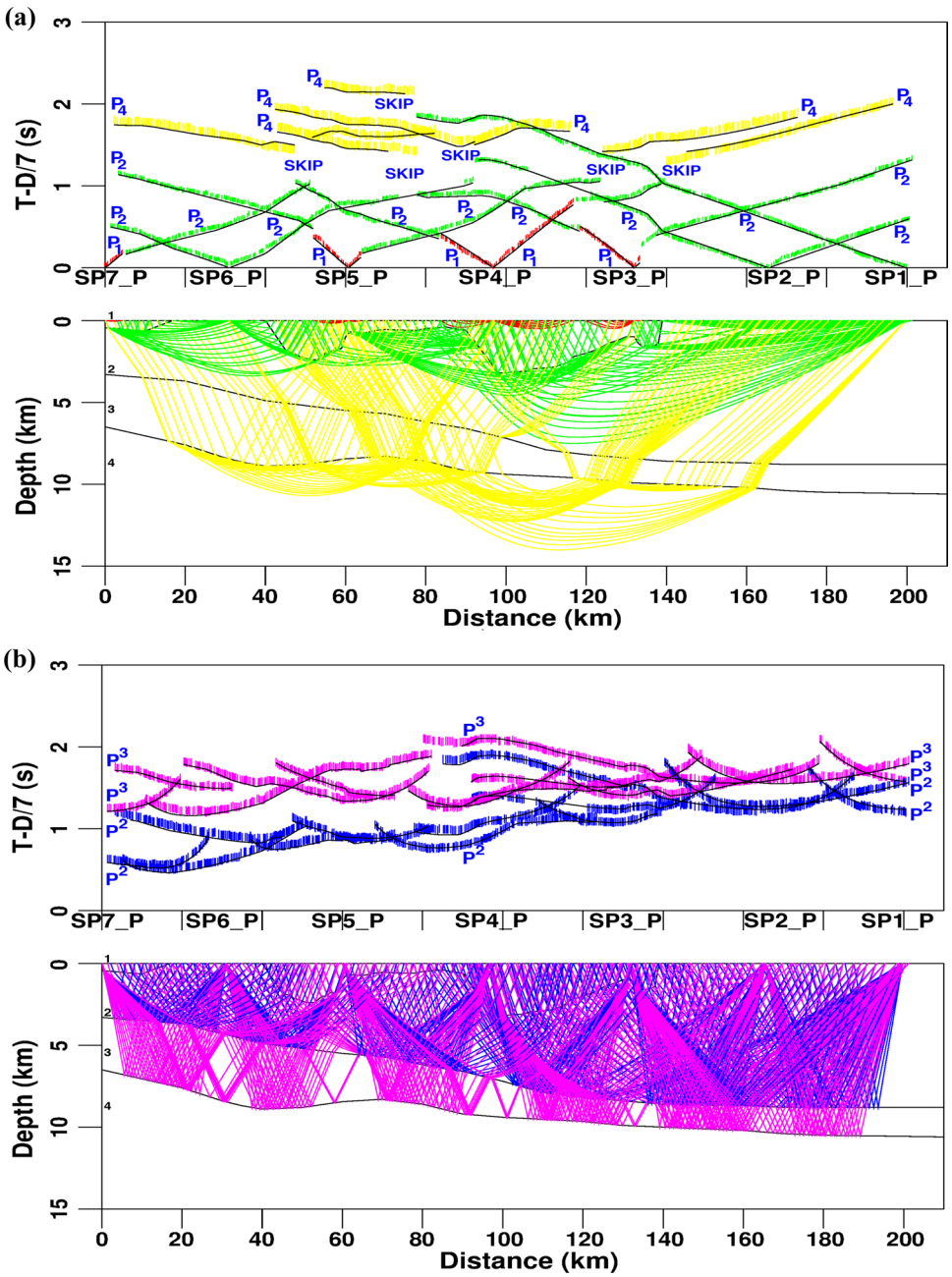

Fig. 6 The ray-trace inversion of *P*-wave **a** first-arrival refraction and **b** reflection traveltime data showing rays traced through each layer of the final *P*-wave velocity model derived from all the shot points SP1 to SP7 along the seismic profile. The picked first-arrival refraction (P_1, P_2, P_4) and reflection (P^2, P^3) traveltime data are shown as colored bars for all the SPs and the corresponding computed responses indicated as solid black line superimposed on the observed data to indicate the nature of traveltime fit (top panels of **a** and **b**) obtained by ray-trace inversion through each layer (marked by the layer number 1, 2, 3 and 4, respectively) of the velocity model derived (bottom panels of **a** and **b**). The traveltime data (top panels of **a** and **b**) are plotted in the time scale with 7.0 km/s reduction velocity. The traveltime skip observed in the first-arrival data for all the SPs are marked as SKIP, which indicates the presence of low-velocity-layer (LVL) along the profile (layer number 3) shown in the bottom panels of **a** and **b**

RMS traveltime residual decreases by fifty percent after the first nonlinear iteration, which indicates that the inversion is neither trapped in a local minimum nor violates the linear assumptions. The data fit is optimum and achieved with chi-square (χ^2) of 1.0. The ray-trace inversion results of seismic refraction and reflection data (*P*- and *S*-waves) for all SPs of the seismic profile acquired in DC (Fig. 1a) are shown with the respective V_P and V_S models derived (Figs. 6, 7, 8 and 9). The inversion takes into account normal forward modeling with layer-stripping technique (Zelt 1999) using the well constrained starting pseudo-2-D velocity models (Fig. 5) derived independently from the corresponding 1-D inversion of *P*-and *S*-wave data (Fig. 4). The chosen parameters such as damping factor of 1.0, a priori error of 0.1 km/s for velocity and 0.1–0.2 km for boundary nodes are used for the ray-race inversion (Zelt and Smith 1992). Since the same source generates *P*- and *S*-wave seismic data due to mode conversion, the recorded data from the different layers should have a common seismic boundary for each layer. Hence, the mutual adjustment has been made to fix the differences of the interface depths for individual layer to derive the final ray-trace inversion V_P and V_S models (Figs. 7 and 9)

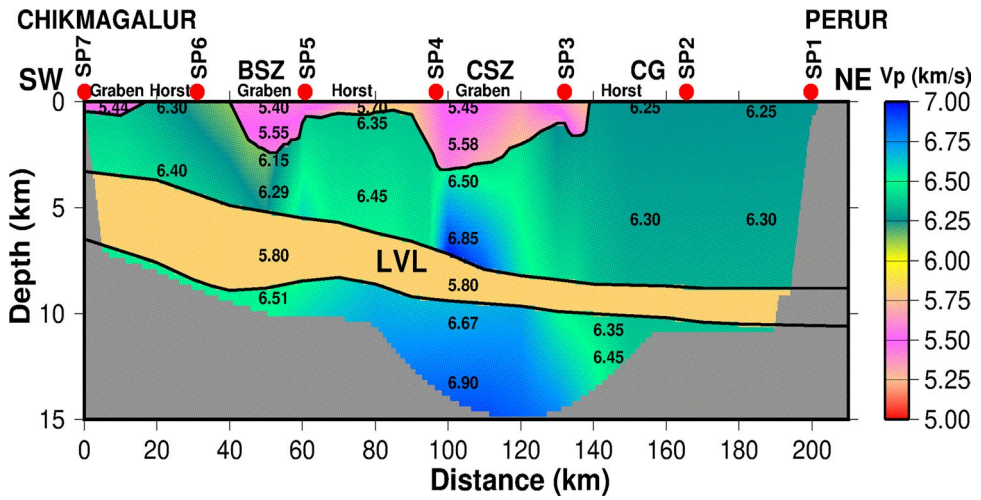

Fig. 7 The *P*-wave upper-crustal velocity model (V_P) obtained along the Perur–Chikmagalur 3-C seismic profile in the Dharwar Craton using ray-trace inversion of radial component *P*-wave first-arrival refraction and reflection traveltime data (Fig. 6). The SP locations along the profile are marked as red dots on the top of the model with corresponding label and the velocity variation is shown in color scale along with average velocity values (km/s) indicated (6.30). The regions not sampled by rays (Fig. 6) are shaded in gray color. BSZ, Bababudan Shear Zone; CSZ, Chitradurga Shear Zone; CG, Closepet Granite

with optimum traveltime fit along the seismic profile (Figs. 6 and 8).

The main requirement of the traveltime fit with respect to the corresponding structures of the velocity model is picking uncertainty of different phases of the observed data (e.g., *P*- and *S*-wave traveltime picks as shown in Table 4). The misfit of the data is controlled by the χ^2 parameter, which should be close to 1.0. For optimum traveltime data fit of the respective phases, the corresponding RMS traveltime residuals obtained should be close to the picking uncertainties of that particular phase (e. g., P^2, P_4 and S^2, S_4, respectively) along with the normalized χ^2 misfit should be close to 1.0 as shown in Table 4. The inversion halts once the misfit parameter becomes 1.0 and the data fit is obtained within the assigned uncertainties (Zelt and Smith 1992; Zelt 1999). In this study, altogether 9771 traveltime picks (refraction and reflection) of *P*- and *S*-waves for seven SPs along the 3-C seismic profile in DC are inverted using ray-trace inversion technique (Fig. 1a). The traveltime data picked (*P*- and *S*-waves) for first-arrival refraction phases (P_1, P_2, P_4 and S_1, S_2, S_4) and reflection phases (P^2, P^3 and S^2, S^3) from top and bottom of the LVL are used for traveltime inversion (Table 4). The data picked are shown for seven SPs as a measure of data quality along with the phases picked using colored dots (Figs. 2, 3, S1 and S2). The synthetic responses computed from the final velocity models (Figs. 7 and 9) along the profile using ray-trace inversion of first-arrival seismic refraction and reflection data picked are superimposed on the respective shot gathers as example (Figs. 2, 3, S1 and S2) to show the nature of traveltime fit (Figs. 6 and 8).

P-wave velocity model (V_P)

The V_P model obtained from inversion of *P*-wave seismic refraction and reflection traveltime data (Fig. 6) is shown in Fig. 7. Total 5013 number of *P*-wave traveltime data picks are used for inversion having RMS residual of 0.046 s and χ^2 of 1.087 (Table 4). The favorable V_P model (Fig. 7) developed from inversion of *P*-wave data has four layers constrained independently from 1-D (Fig. 4a) and pseudo-2-D models (Fig. 5a). The top (0.5–2.5 km) layer (mainly volcano–sedimentary rocks) with velocities of 5.40–5.70 km/s constitutes the first layer. The corresponding *P*-wave velocity of second layer (basement) varies from 6.15 to 6.50 km/s (0.02–0.06 s^{-1} gradient) with lateral and vertical velocity variations, which is relatively thick (2.5–8.5 km) toward NE of the profile. The basement is exposed within 20–40 km, 60–90 km and 140–210 km forming horst structures along the profile. Based on the *P*-wave velocity variations (Fig. 7), the basement layer mainly corresponds to mafic materials of high-grade greenstones toward SW and low-grade greenstones of felsic materials toward NE (Fig. 1a). The presence of high V_P (6.85 km/s) basement materials extending to a depth of 3–7 km forming the CSZ represents anomalous rock types formed due to exhumation of mid- or lower-crustal mafic materials at shallow depth (Fig. 7). The NE dipping LVL below the basement represents a conspicuous layer with V_P of 5.8 km/s forms a zone of detachment. The LVL is relatively thick (3.5 km) in the SW as compared to NE, which is gradually thinning (2.0 km). This is constrained from the amount of traveltime skips present in all the SPs

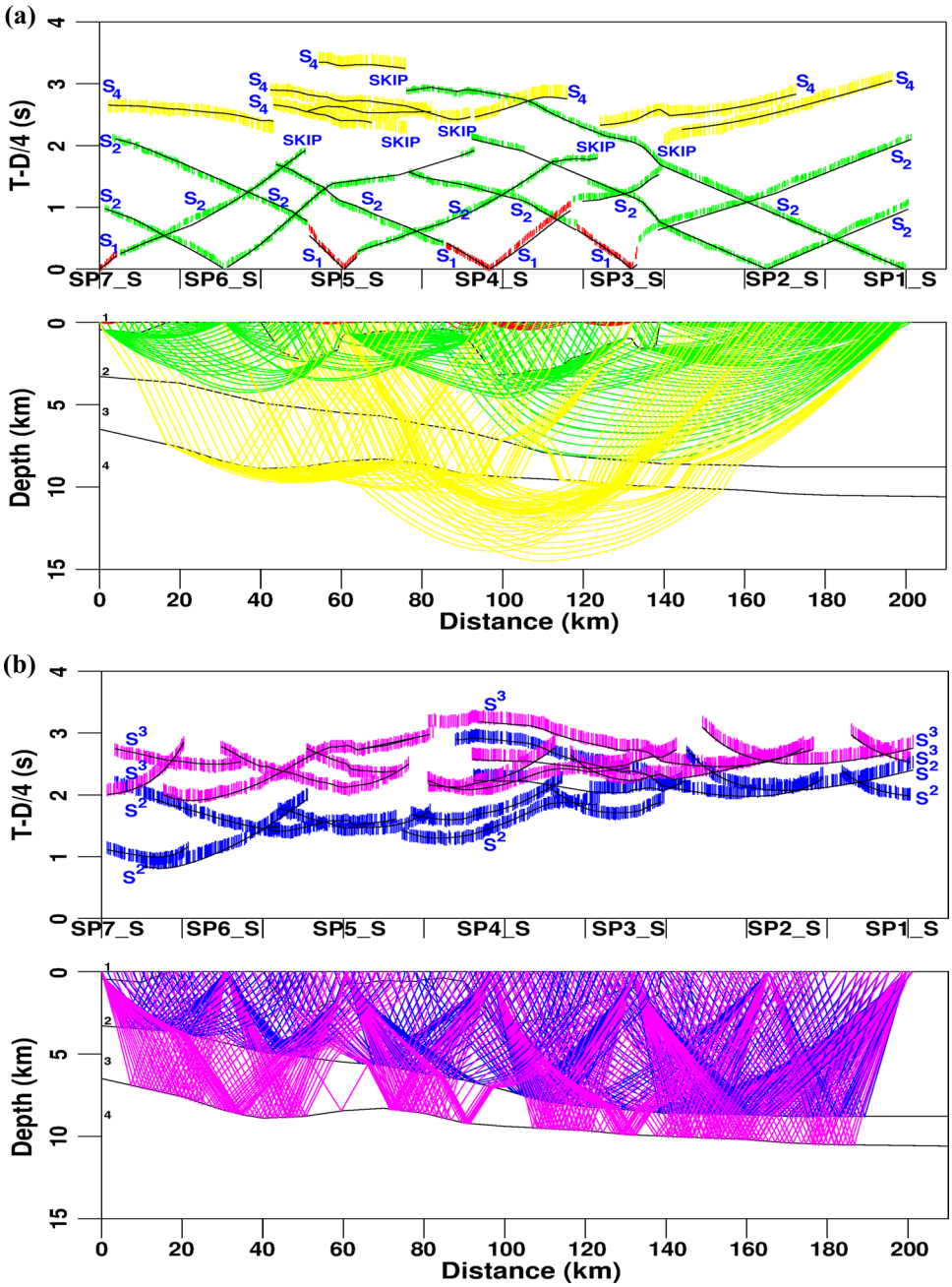

Fig. 8 The ray-trace inversion of *S*-wave **a** first-arrival refraction and **b** reflection traveltime data showing rays traced through each layer of the final *S*-wave velocity model derived from all the shot points (SP1 to SP7) along the same profile. The corresponding picked first-arrival refraction and reflection traveltime data (colored bars with phases S_1, S_2, S_4 and S^2, S^3, respectively) for all the SPs and the computed responses (solid black line) for each layer (marked by layer number 1, 2, 3 and 4) of the model derived (bottom panel of **a** and **b**) are superimposed to indicate the nature of traveltime fit (top panel of **a** and **b**) plotted in the time scale with 4.0 km/s reduction velocity. The traveltime skip observed in the first-arrival data for all the SPs is marked as SKIP, which indicates the presence of LVL along the profile (bottom panel of **a** and **b**)

and corresponding inversion of first-arrival traveltime data (Figs. 2, S1, 4a and 6a). The velocity of the fourth layer varying from 6.3 to 6.9 km/s (0.01–0.03 s^{-1} gradient) represents high-velocity mafic materials formed at deeper crust and emancipated through CSZ due to intense shearing, which are mainly exposed at shallow level of the Dharwar Craton (Fig. 7).

S-wave velocity model (V_S)

The V_S model is derived along the same profile from inversion of *S*-wave seismic refraction and reflection traveltime data (Figs. 8 and 9). The preferred *S*-wave velocity model (Fig. 9) has four layers independently obtained with the help of 1-D (Fig. 4b) and pseudo-2-D models (Fig. 5b). Total 4758 *S*-wave phases (refractions and reflections) picked for all the SPs are used for traveltime inversion (Fig. 8) having RMS residual of 0.089 s and χ^2 of 1.108 (Table 4).

The upper-crustal structure of V_S model (Fig. 9) shows same four layers as obtained for V_P model (Fig. 7) with corresponding V_S varying from 3.24 to 3.98 km/s. Similar horsts and grabens are delineated with relatively high V_S of 3.24–3.32 km/s for the first (top) layer. There is presence of both vertical and lateral V_S variations (3.50–3.65 km/s) in

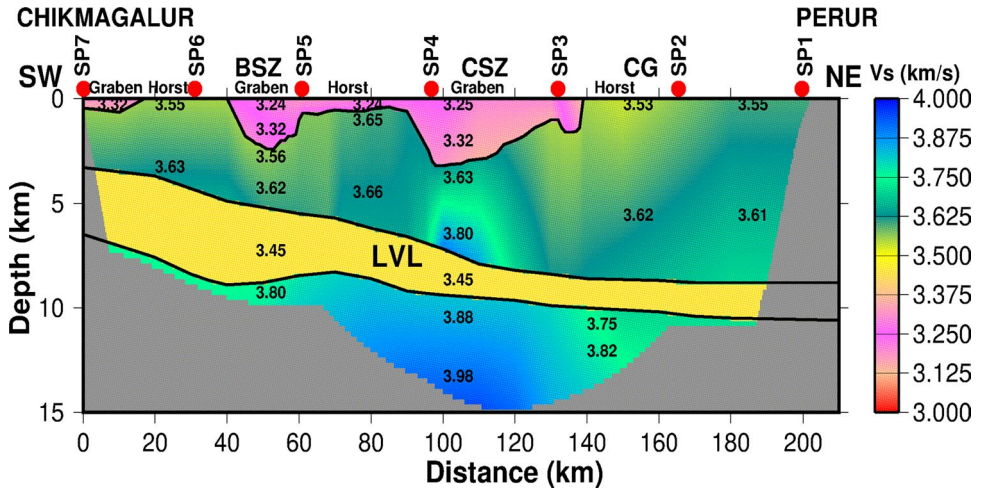

Fig. 9 The *S*-wave upper-crustal velocity model (V_S) obtained along the same 3-C seismic profile in the Dharwar Craton using ray-trace inversion of radial component S-wave first-arrival refraction and reflection traveltime data (Fig. 8). The SP locations along the profile are marked as red dots on top of the model with corresponding label and the velocity variation is shown in color scale along with average velocity values (km/s) indicated (3.62). The regions not sampled by rays (Fig. 8) are shaded in gray color. BSZ, Bababudan Shear Zone; CSZ, Chitradurga Shear Zone; CG, Closepet Granite

the second layer (Fig. 9) similar to the corresponding V_P model representing the crystalline basement with felsic granites and gneisses in the NE to mafic rocks predominant toward SW of the profile. The high-velocity (3.80 km/s) zone corresponding to CSZ sandwiches WDC and EDC blocks with a clear demarcation between these two blocks. It could be intrusions of mid-crustal rocks with large-scale exhumation at shallow depths forming horst structure (Fig. 9). The presence of the LVL (third layer) is evident and also constrained from the *S*-wave traveltime skips observed (Figs. 3, S2, 4b and 8a), although the *S*-wave data quality is little noisy (Figs. 3, S2). The LVL (3.45 km/s) is constrained using 1-D inversion of *S*-wave first-arrival refraction traveltime picks (Fig. 4b). The starting V_S (3.35 km/s) for the LVL was obtained from the corresponding V_P (5.8 km/s) using fixed $\sigma = 0.5\left[\frac{\gamma^2-2}{\gamma^2-1}\right]$ of 0.25 for the crust, where $\gamma = V_P/V_S = 1.732$. Then the V_S of the LVL was varied from 3.35 to 3.65 km/s at 0.10 km/s interval to fit the *S*-wave first-arrival traveltime data for different SPs by using the same DLS inversion method (Zelt and Smith 1992; Sain and Kaila 1994; Behera et al. 2004). The traveltime skips of all the SPs and corresponding inversion of *S*-wave reflection phases along the profile obtained from top and bottom of the LVL are used to determine the thickness and velocity of this layer with optimum fit of the picked *S*-wave traveltime data. The corresponding *S*-wave velocity for the LVL (Fig. 4b) is computed as 3.45 km/s, obtained similarly to the *P*-wave traveltime data inversion. The fourth layer shows V_S variation of 3.75–3.98 km/s and is composed of mainly granite–gneiss–greenstones (Fig. 9).

V_P/V_S, σ and lithology of upper crust

The V_P and V_S models (Figs. 7 and 9) of the upper crust create well constrained V_P/V_S and σ models (Figs. 10 and 11) of the Dharwar Craton. This study deals with modeling and inversion of both refraction and reflection traveltime data (*P*- and *S*-waves) to decipher upper-crustal rock compositions and lithological variations in WDC and EDC blocks of DC. The computation of σ (Poisson's ratio) values is made from each node of the derived V_P and V_S models (Figs. 7 and 9) along the profile. The variations of V_P/V_S (1.63–1.80) and σ (0.20–0.28) along the seismic profile (Figs. 10 and 11) indicate the nature of lithological and compositional distinctions, which are not deciphered from the independent velocity (V_P and V_S) information (Figs. 7 and 9). The first (top) layer (volcano–sedimentary) with graben structures (Fig. 10) has very low values of V_P/V_S (1.63–1.68) attributed to quartz-rich lithologies (Johnston and Christensen 1993). The Poisson's ratio variation of the first layer (0.20–0.25) is shown in Fig. 11. The V_P/V_S variations of the second layer (1.72–1.80) with corresponding variation of σ from 0.25 to 0.28 represent the shallow upper-crustal crystalline basement. This indicates distinct classification of different rock types with the presence of anomalously high V_P/V_S (1.80) and σ (0.28) values below the CSZ representing a compositional boundary of the Dharwar Craton. The V_P/V_S of 1.74–1.76 represents felsic to intermediate composition of rocks and 1.75–1.78 represents mafic compositions, respectively, with comparatively high values (1.79–1.80) for the CSZ with the presence of mylonites and high-strain orthogneisses formed due to intense shearing and exhumation

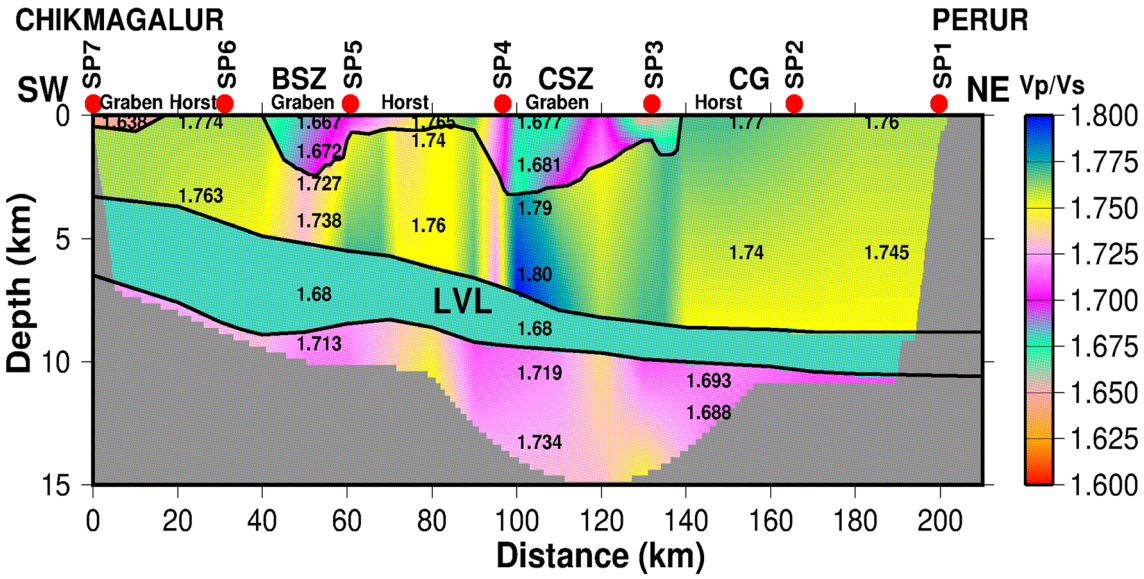

Fig. 10 V_P/V_S image of the upper crust computed along the seismic profile of study. The SPs are shown as red dots on the top with labels. The V_P/V_S variation is shown in color scale and numbers indicating average V_P/V_S values (1.74). Regions not sampled are shaded in gray color

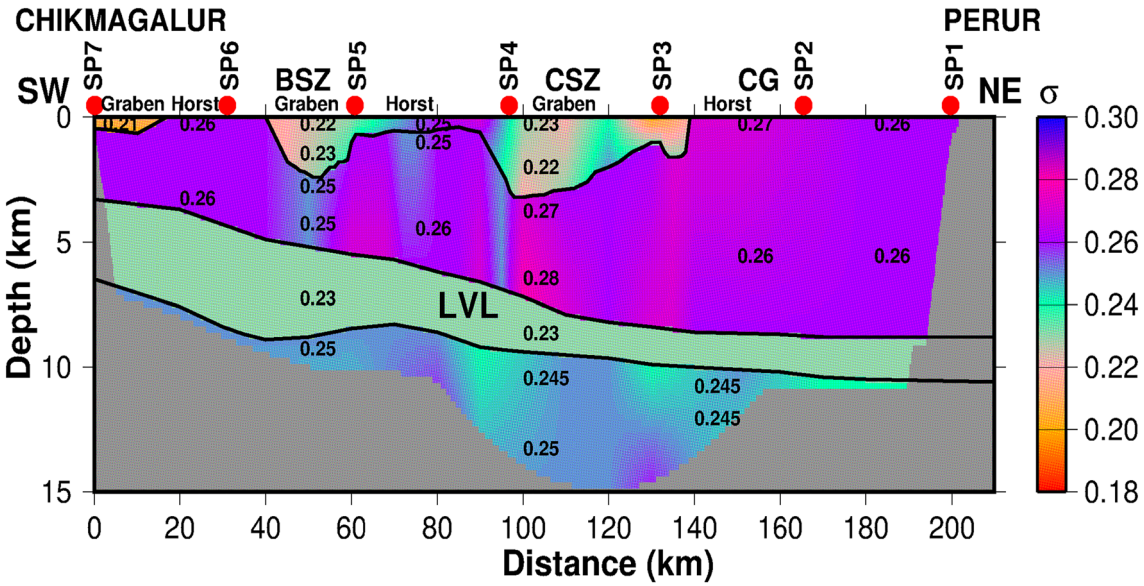

Fig. 11 Poisson's ratio (σ) image of the upper crust computed along the seismic profile of study. SPs are shown as red dots on the top with labels. The variation of σ is shown in color scale and by numbers indicating its average values (0.26). Regions not sampled correlating V_P/V_S (Fig. 10) are shaded in gray color

(Chadwick et al. 2000). The major schist zones are commonly associated with mylonitized granites and gneisses. The extension of the high-strain zone is mapped for 20-km in this region with a clear extension along the strike for 110-km having partially exposed rocks (Chadwick et al. 2000). The variation of σ (0.27–0.28) indicates emancipation of mid-to-lower crustal rocks through the excellent conduits formed in these highly strained and distorted shear zones of the Dharwar Craton. These rocks are exhumed in the upper crust, which are mainly of mafic to ultramafic compositions forming horst structures. The LVL (low V_P and V_S) was developed in the upper crust mainly composed of quartz-pebbles and meta-conglomerates. This layer is formed as a result of high pressure and temperature conditions prevailed in this region of DC because of emancipation of mid-crustal materials at shallow level. The computed values of V_P/V_S

and σ are 1.68 and 0.23, respectively, for the LVL, which forms a major unconformity called upper-crustal detachment zone. The upper-crustal rocks corresponding to CSZ below the LVL although have higher V_P (6.67–6.90 km/s) and V_S (3.88–3.98 km/s), but the corresponding V_P/V_S varies from 1.719 to 1.734 and σ varies from 0.245 to 0.250 (Figs. 7, 9, 10 and 11). The V_P/V_S and σ variations along the seismic profile (Fig. 1a) provide a better control of the upper-crustal rock compositions along with the shallow V_P and V_S models in comparison to the only vertical *P*-wave velocity model obtained previously by crustal study of DC (Rao et al. 2015a, b). The variation of σ for the crustal rocks (0.20–0.35) mainly depends on the rock compositions, mineral assemblages and tectonic settings of similar cratonic provinces of the world (Fernandez-Viejo et al. 2005; Rumpfhuber and Keller 2009). The age and silica contents of the rocks influence the average value of σ, which generally increases with age and decreases with the presence of silica content within the different rocks. The average value of σ in silica-rich felsic rocks such as quartz becomes very low because of extremely low value (0.09) of Poisson's ratio (Zandt and Ammon 1995; Rumpfhuber and Keller 2009). The anomalous high V_P/V_S (1.80) and σ (0.28) of CSZ forms a distinct compositional division for EDC and WDC and depicts clearly lateral and vertical variations (Figs. 10 and 11). This anomalous body with increase of V_P/V_S and σ is linked to important shear zones such as CSZ and BSZ along the 3-C seismic profile of DC in southern India. These shear zones act as the conduits for the flow of deep magmatic fluids to shallow level as well form important site for precious mineral deposits.

Model validation and assessment

The model validation and assessment mainly govern the stability and accuracy of the derived final velocity model. The following important criteria are necessary for deriving the final velocity model from inversion of traveltime data such as: (1) χ^2 misfit and traveltime residuals, (2) RMS traveltime misfit, (3) resolution and uncertainty estimates, and (4) amount of ray coverage as a measure of hitcounts or ray density (Zelt and Smith 1992; Zelt 1999). The corresponding measured values of these parameters (statistical estimates) for the final velocity models derived for both V_P and V_S are shown in Table 4 along with the respective fits of *P*-wave (Fig. 6) and *S*-wave data (Fig. 8). The ray-trace inversion results are shown with the help of V_P (Fig. 7) and V_S (Fig. 9) models derived for the 3-C seismic profile of DC (Fig. 1a).

Resolution and uncertainty estimate

The most important parameters for model assessment are computation of resolution and uncertainty estimates. The resolution and uncertainty values of the derived model are computed from the respective diagonal elements of the resolution and covariance matrices (Zelt and Smith 1992). The corresponding values of the resolution matrix vary from 0 to 1. However, the computed values greater than 0.5 indicate improved resolution, lateral and vertical averaging of the true structures of the subsurface earth model. This is mainly governed by the ray coverage (Figs. 6 and 8) of the derived velocity model along with the measure of true and inverted parameters. The final resolution matrices computed for both V_P and V_S models are shown along the profile (Figs. 12 and 13). Note that same damping parameter of 1.0 is kept during the estimate of resolutions for both velocity (pink dots) and depth nodes (squares), respectively. The resolution values computed are more than 0.7 for most of the nodes due to sufficient ray coverage through the V_P and V_S models along the profile (Figs. 6 and 8). However, the low resolutions (less than 0.5) in few locations at certain depths or toward end of the profile are due to poor ray coverage. This indicates that both V_P and V_S models are well resolved (Figs. 12b and 13b) and hence consistent.

The uncertainties are computed from covariance matrix having a posteriori model constraint (Tarantola 1987; Zelt and Smith 1992). These errors do not consider any bias of the model parameters since they represent the lower bound of the true model parameter and are related mainly to the traveltime picking uncertainties only. The other plausible errors playing important role for uncertainty estimates of the model are (1) mis-identification of different phases, (2) 3-D structures used for modeling as 2-D, (3) receiver geometry and (4) improper parameterization (Zelt and Smith 1992). Generally linear assumption is made for analysis of covariance matrix. But a uni-parameter uncertainty test is performed for considerable insight of the model constraints, which mainly controls the nonlinear traveltime inversion (Zelt and Smith 1992; Zelt 1999). Since the error analysis of all the velocity and boundary nodes of the derived final model could take very long time, a single representative node is used to compute the absolute uncertainty of each layer (Zelt 1999; Behera et al. 2004; Behera and Kumar 2022). The absolute uncertainty estimates for the V_P (6.67 km/s) and V_S (3.82 km/s) nodes of the upper crust are shown (Figs. 12c and 13c) as well as the corresponding depth node (9.4 km) of the fourth layer (Figs. 12d and 13d) at 100 km profile distance near CSZ. The absolute uncertainty of V_P spans from −0.21 to +0.19 km/s and V_S spans from −0.14 to +0.18 km/s for 50 ms and 100 ms RMS residuals, respectively. Also, the upper-crustal boundary (fourth layer) depth node at 9.4 km shows the absolute depth uncertainties of *P*- and *S*-waves span from −1.0 to +0.9 km and −0.7 km to +0.8 km for respective 50 ms and 100 ms RMS residuals (Figs. 12d and 13d). Similarly, the computed uncertainty values of selected V_P and V_S nodes of different

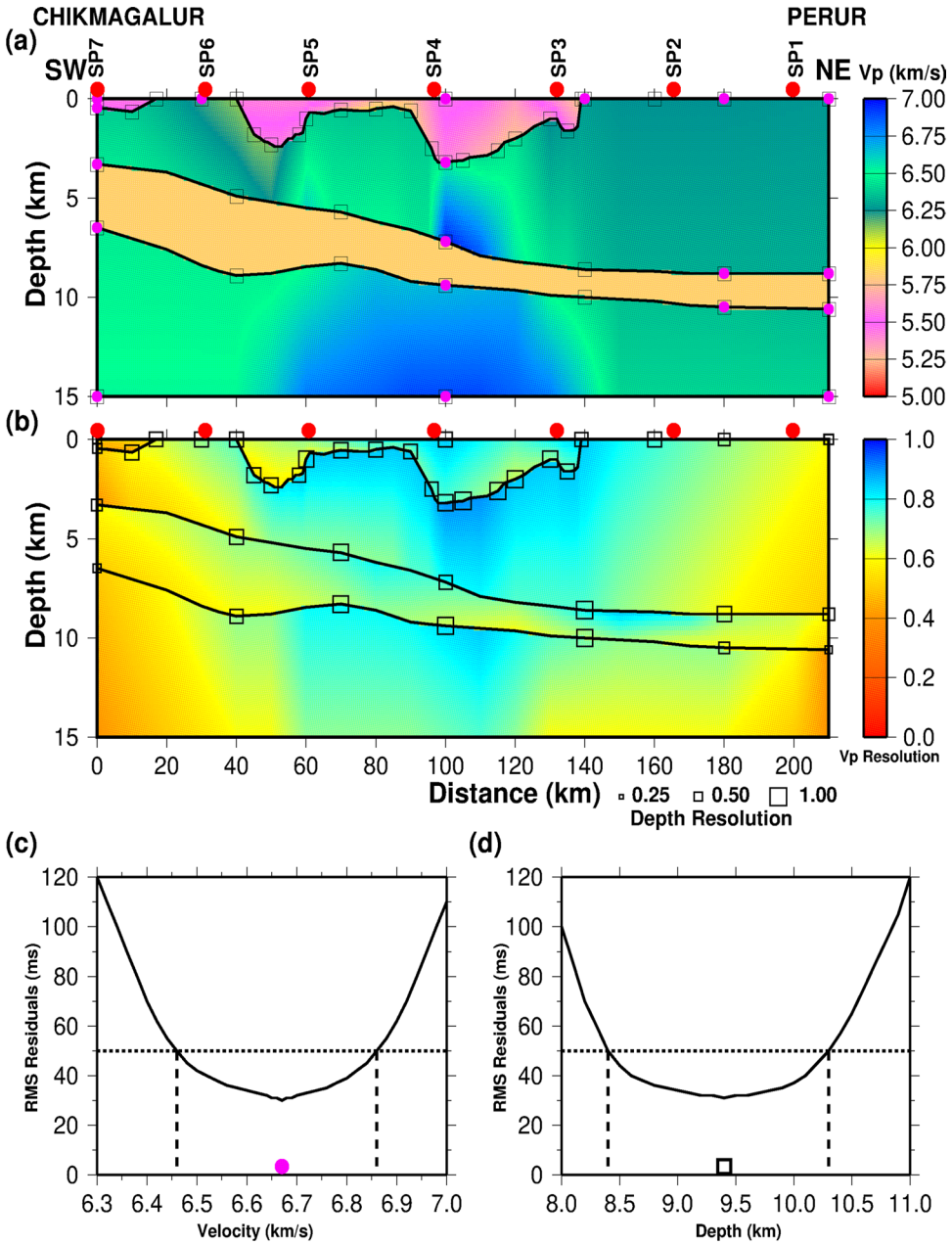

Fig. 12 Resolution and absolute uncertainty estimates of the final *P*-wave velocity model along the seismic profile showing **a** velocity (solid pink dots) and boundary (squares) nodes representing the model parameterization with the corresponding *P*-wave velocity variation (V_P) through the model, **b** velocity and depth resolutions for each node represented by variations in color with corresponding color scale and size of the squares, respectively, **c** RMS traveltime residual as a function of velocity perturbation (solid curve) with respect to the velocity node (6.67 km/s) of the fourth layer at 9.4 km depth and 100 km distance having absolute velocity uncertainty varying between 6.46 and 6.86 km/s (−0.21 km/s to +0.19 km/s) corresponding to 50 ms traveltime residual, **d** RMS traveltime residual as a function of depth perturbation (solid curve) with respect to the same depth node (at 9.4 km) having absolute depth uncertainty varying between 8.4 and 10.3 km (−1.0 km to +0.9 km) corresponding to 50 ms traveltime residual

layers in the upper crust vary from ±0.18 to ±0.15 km/s. The corresponding depth uncertainties at chosen nodes of different layers in the upper crust range from ±0.82 km for *P*-wave and ±0.77 km for *S*-wave along the profile. It is true that there is a trade-off between resolution and uncertainty estimates and if the uncertainty is more, then velocity resolution will decrease and vice versa. Also, there will be large velocity uncertainty if the ray-coverage is very poor through the velocity model derived due to very sparse receivers or very low SNR. The higher uncertainty values also eliminate the significance of any lateral variations in V_P/V_S or the Poisson's ratio (Musacchio et al. 1997). In our case, we have sufficient ray coverage through the V_P and V_S models from all the SPs with good SNR (Figs. 2, 3, S1, S2, 6 and 8); hence, the velocity uncertainty obtained for the upper crust is reasonable. Similarly, the absolute uncertainty values computed for V_P/V_S varied from −0.06 to +0.07 and the corresponding uncertainties of the σ varied from −0.04 to +0.03 taking into consideration the respective velocity nodes (Figs. 12a and 13a). The same value of 1.0 damping parameter kept for all these tests, which indicate that V_P, V_S, V_P/V_S, and σ models derived are well resolved and reliable.

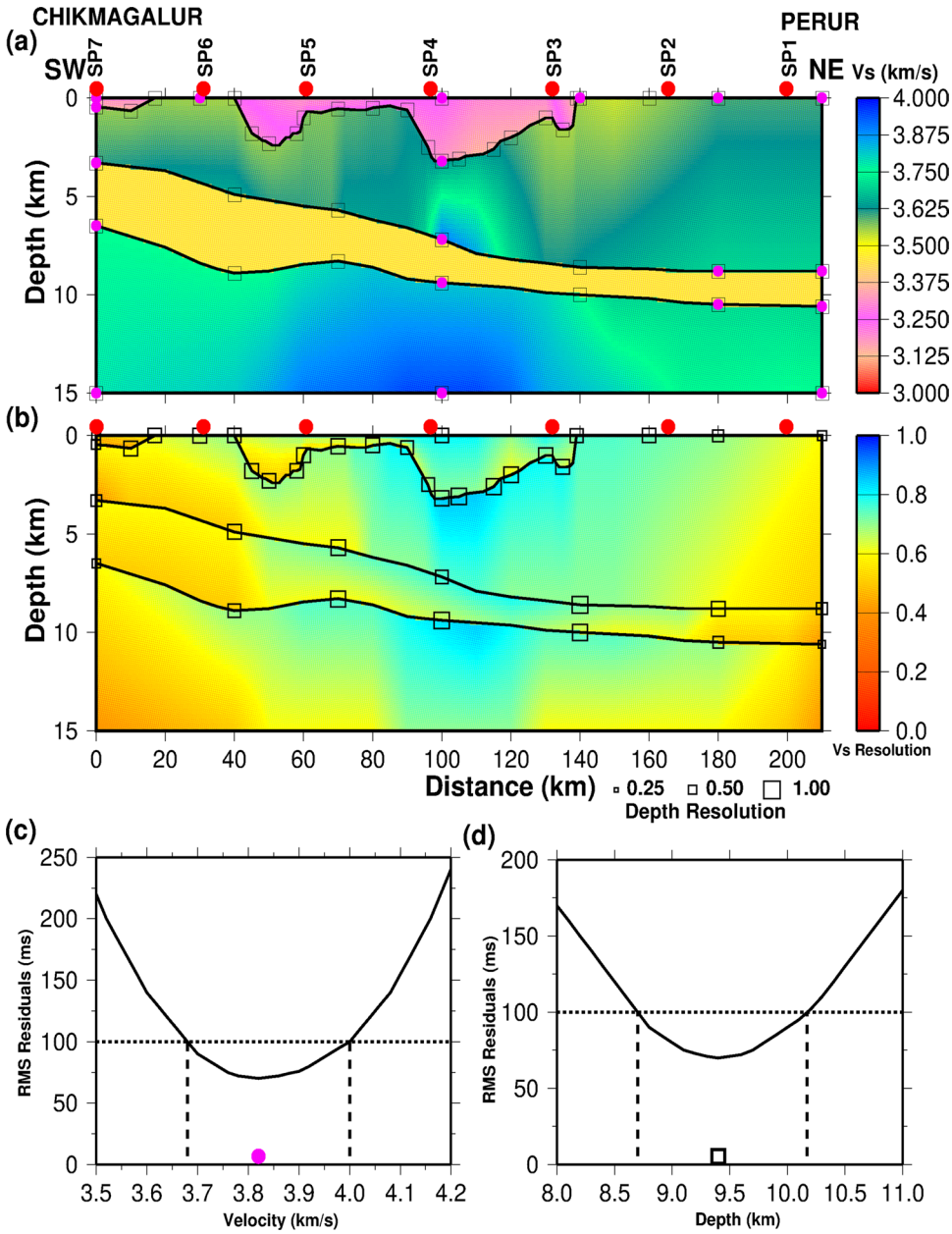

Fig. 13 Resolution and absolute uncertainty estimates of the final *S*-wave velocity model along the seismic profile showing **a** velocity (solid pink dots) and boundary (squares) nodes representing the model parameterization with the corresponding *S*-wave velocity variations (V_S) through the model, **b** velocity and depth resolutions for each node represented by variations in color with color scale and size of the squares, respectively, **c** RMS traveltime residual as a function of velocity perturbation (solid curve) with respect to the velocity node (3.82 km/s) of the fourth layer at 9.4 km depth and 100 km distance having absolute velocity uncertainty varying between 3.68 and 4.00 km/s (−0.14 km/s to +0.18 km/s) corresponding to 100 ms traveltime residual, **d** RMS traveltime residual as a function of depth perturbation (solid curve) with respect to the same depth node (at 9.4 km) having absolute depth uncertainty varying between 8.7 and 10.2 km (−0.7 km to +0.8 km) corresponding to 100 ms traveltime residual

Ray density or hitcount estimate

The measure of ray density or hitcounts (Hits) for each cell of the model is governed by the number of rays passing through the model. The hitcounts increase with increasing quantity of rays penetrated through cells as the cell size increases (Zelt 1999). On the other hand, the resolution of the model decreases. Hence, the cell size of the model is optimally chosen so that rays should pass through the cells moderately. For computation of hitcounts of both V_P and V_S upper-crustal models of the Dharwar Craton, the optimum cell size is chosen as 0.5 km × 0.5 km (Fig. 14). The upper-crustal V_P and V_S models show hitcounts (> 20) with different colors (orange, yellow, green and cyan) in the corresponding hitcount plots (Fig. 14). Hence, both V_P and V_S models are properly assessed by the nature and size of refraction and reflection ray propagation within the models as well as estimates of velocity and depth uncertainties using different velocity and boundary nodes (Behera et al. 2004; Behera 2011b; Behera and Sarkar 2011; Behera and Sen 2014; Behera and Kumar 2022).

Discussion and interpretation of the results

The EDC and WDC blocks show diverse seismic elements with prominent structural feature or terrain boundary like CSZ dividing these two blocks of DC. The corresponding

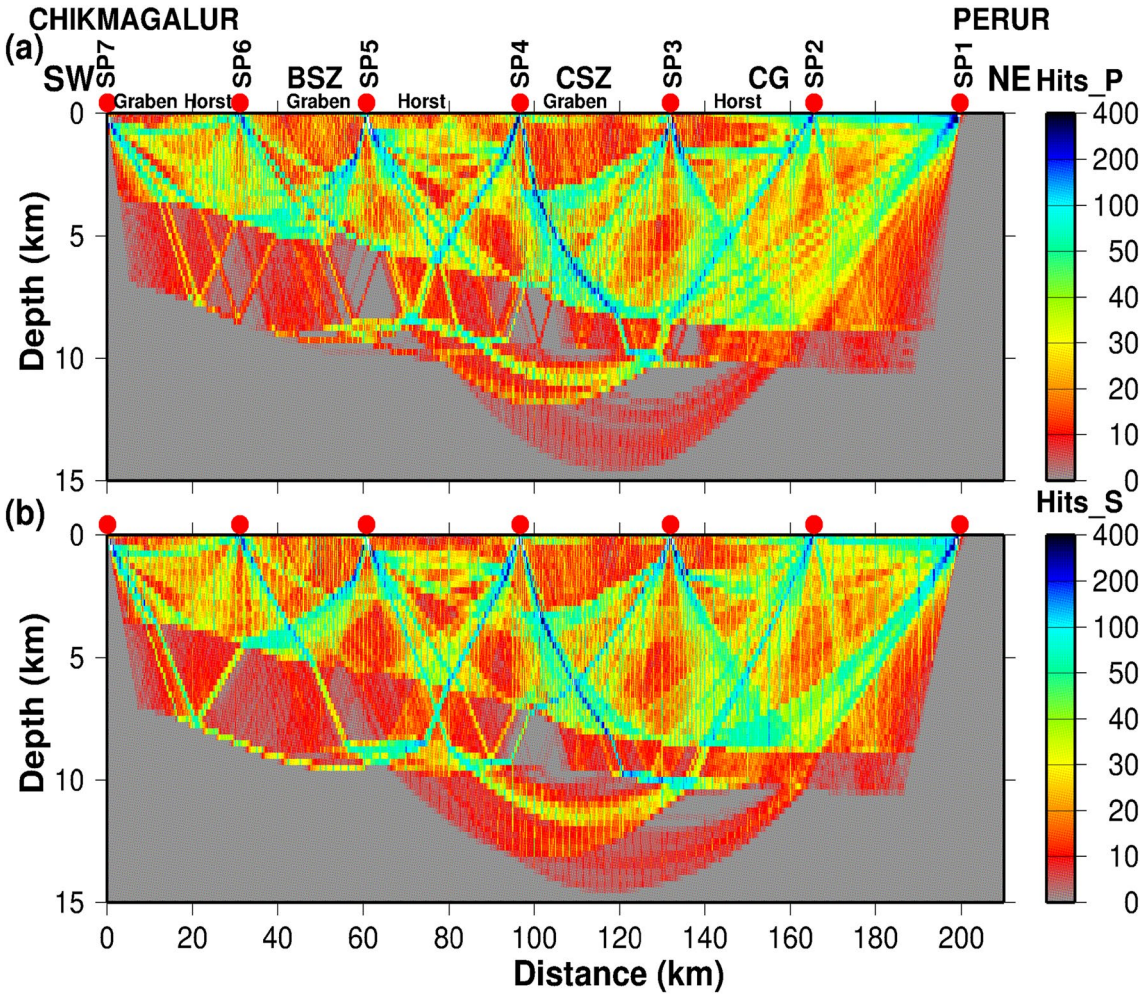

Fig. 14 Ray density or Hits plot of **a** *P*-wave velocity (V_P) model and **b** *S*-wave velocity (V_S) model with respective color scales representing number of rays passing through the chosen cell size (hit counts). The regions not sampled by rays are shaded in gray color, and SPs are shown as red dots with label along the 3-C seismic profile

values of V_P range between 5.40 and 6.90 km/s (Fig. 7) and V_S range between 3.24 and 3.98 km/s (Fig. 9) in the 15-km-thick four-layered upper-crustal *P*- and *S*-wave models derived. The CSZ (major suture zone) in the upper crust of WDC is indicated by a ramp with high V_P (6.85 km/s) and V_S (3.80 km/s) between 90 and 120 km profile distance, as seen in corresponding velocity models (Figs. 7 and 9). From the independent V_P or V_S velocity estimates alone, which generally provide the lateral and vertical variations of velocity, these are not considered as a good proxy for the estimate of the rock compositions. The main issue is that both V_P and V_S values generally fall within a typical range for a particular rock type, which also overlap for different rocks and hence difficult to ascertain the composition of the rocks from V_P or V_S values independently. Since the seismic profile of this study region has been executed in a very hard rock Archean metamorphic terrain, the velocity uncertainty of ±0.15 km/s is considered as more for the upper crust as observed in similar geological terrains of the world (Musacchio et al. 1997). Also, the V_P values computed for the upper crust of Dharwar Craton using the seismic refraction data (single component) along the same profile (Rao et al. 2015a, b) show hardly any lateral velocity variations (e.g., ±0.05 km/s) because they have used data recorded by the vertical component geophones only. The upper crust was modeled in the previous study using only two layers having V_P of 6.0 km/s and 6.3 km/s, respectively, with a significant drop of 0.15 km/s near CSZ (e.g., 5.85 km/s velocity), which are shown as nearly flat horizontal layers (Rao et al. 2015b) without looking into the geological complexity of this region. On the other hand, using the same vertical component *P*-wave data, Rao et al. (2015a) have shown smooth vertical variations of V_P from 5.7 to 6.4 km/s using first-arrival traveltime

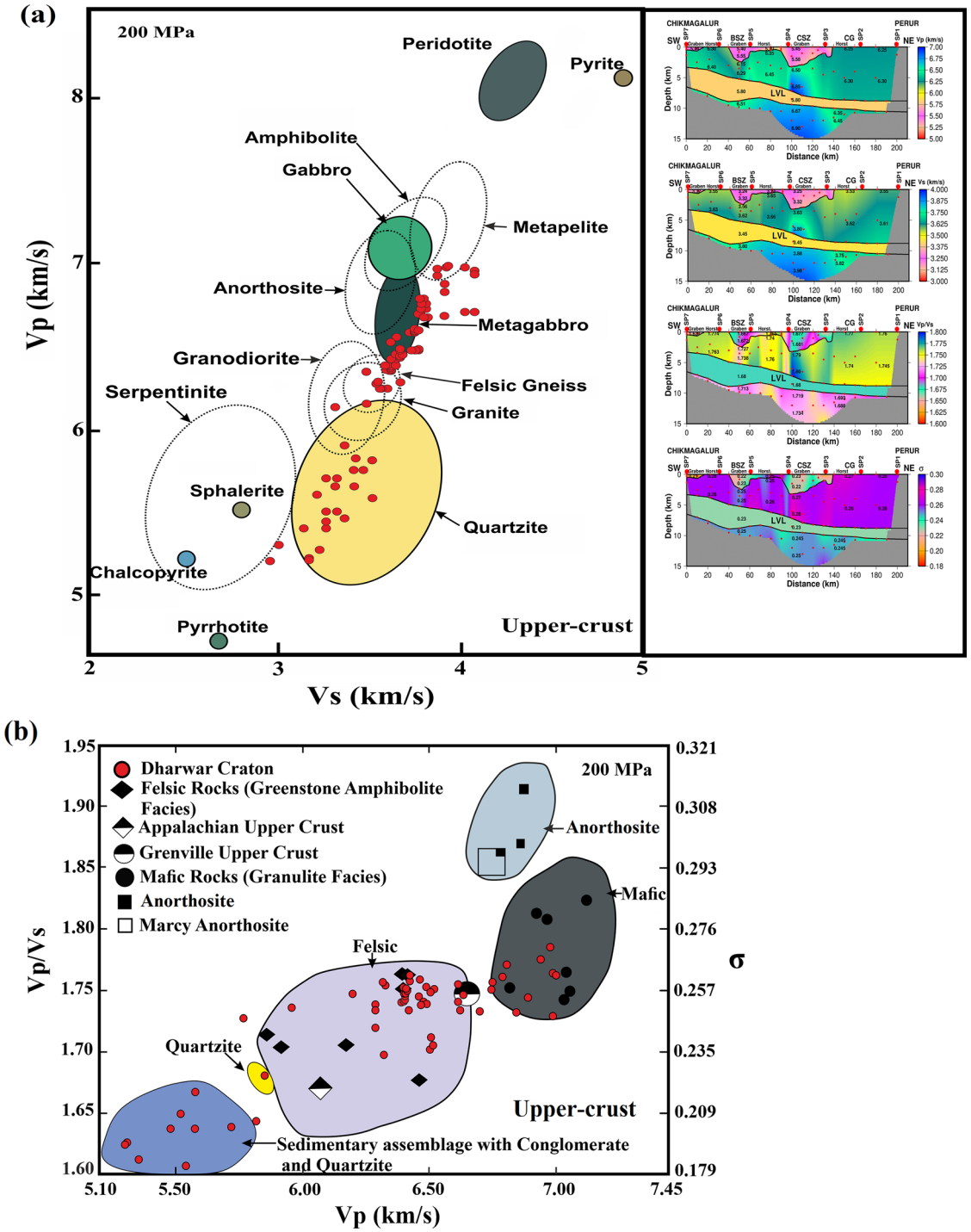

Fig. 15 Upper-crustal rock compositions inferred from this study using *P*- and *S*-wave traveltime data along the 3-C seismic profile of the Archean Dharwar Craton by plotting **a** the computed values of V_P and V_S models (shown as inset with different nodes marked as red dots within the models) are superimposed on the corresponding laboratory measurements of V_P vs V_S data for different upper-crustal rock samples of similar Archean Province (Abitibi Greenstone Belt of Canada) at 200 MPa pressure for comparison of seismic wave speeds in typical rock samples marked as ellipses (Holbrook et al. 1992; Christensen 1996; Snyder et al. 2009; Salisbury et al. 2003; Wang et al. 2005a, b). The major classification of different rock types is shown as ellipses (colored and white) indicated by arrows. **b** V_P/V_S vs V_P computed (red dots) along the profile of study marked on the plot obtained by Musacchio et al. (1997) showing shaded area for group of rocks having similar compositions and similar seismic properties corresponding to the upper crust at 200 MPa. **c** V_P/V_S vs V_S computed (red dots) along the same profile superimposed on the shaded area plot (Musacchio et al. 1997) showing rock compositions at 200 MPa. **d** Relation between the V_P/V_S, Poisson's ratio (σ) and K/μ (ratio of bulk and shear modulus) shown as standard curves (Tatham 1982) and the corresponding computed values (brown circles for σ and blue circles for K/μ) along the profile of study in the Dharwar Craton placed within the standard curves indicating a very good correlation

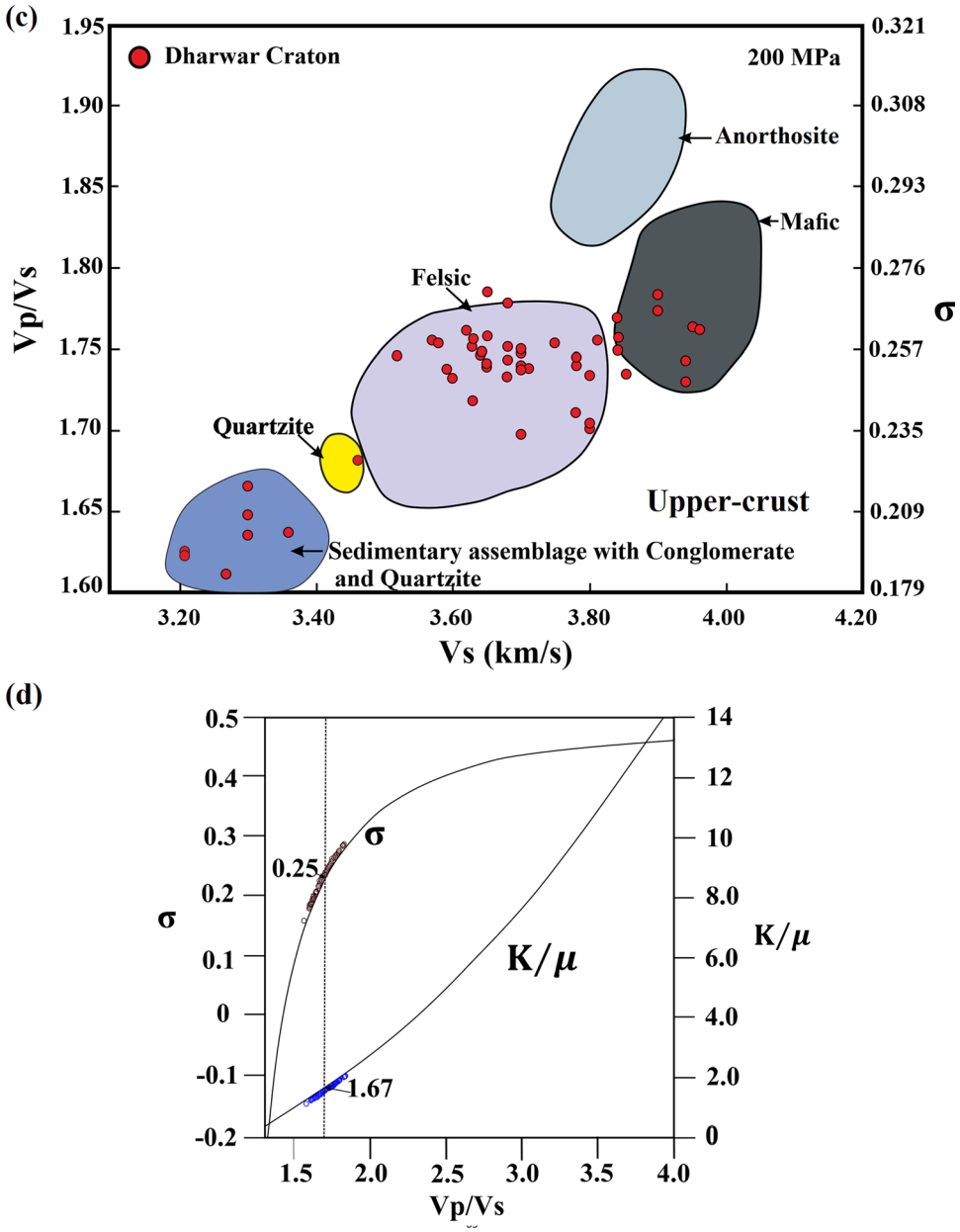

Fig. 15 (continued)

tomography to represent upper-crustal horst and graben only with the help of velocity contours along the same profile.

Although the study region is mainly confined to the Archean terrain of the Dharwar Craton with distinct blocks (EDC and WDC) having different rock compositions and a major shear zone (CSZ) forming a large suture, the vertical component *P*-wave velocity model alone obtained by Rao et al. (2015a, b) could not address the geological complexity of this region correlating the surface exposure of different rocks. However, from the rigorous analysis of 3-C seismic data with modeling and inversion of refraction and reflection traveltime picks, we have derived upper-crustal V_P, V_S, V_P/V_S and σ models of DC (Figs. 7, 9, 10 and 11), which are considered as the most diagnostic of different rock composition, tectonics and subsurface geological structures in this complex geological terrain. Hence, the integrated interpretation of V_P, V_S, V_P/V_S, σ and the bulk modulus (K) and shear modulus (μ) parameters computed in this study (Appendix 2) are used to better constrain the subsurface geology and provide a true assessment of the rock compositions for these two discordant blocks EDC and WDC juxtaposed by the complex suture called CSZ. The CSZ is very prominent in V_P, V_S, V_P/V_S and σ images (Figs. 7, 9, 10 and 11) with relatively high (anomalous) V_P (6.85 km/s), V_S (3.80 km/s),

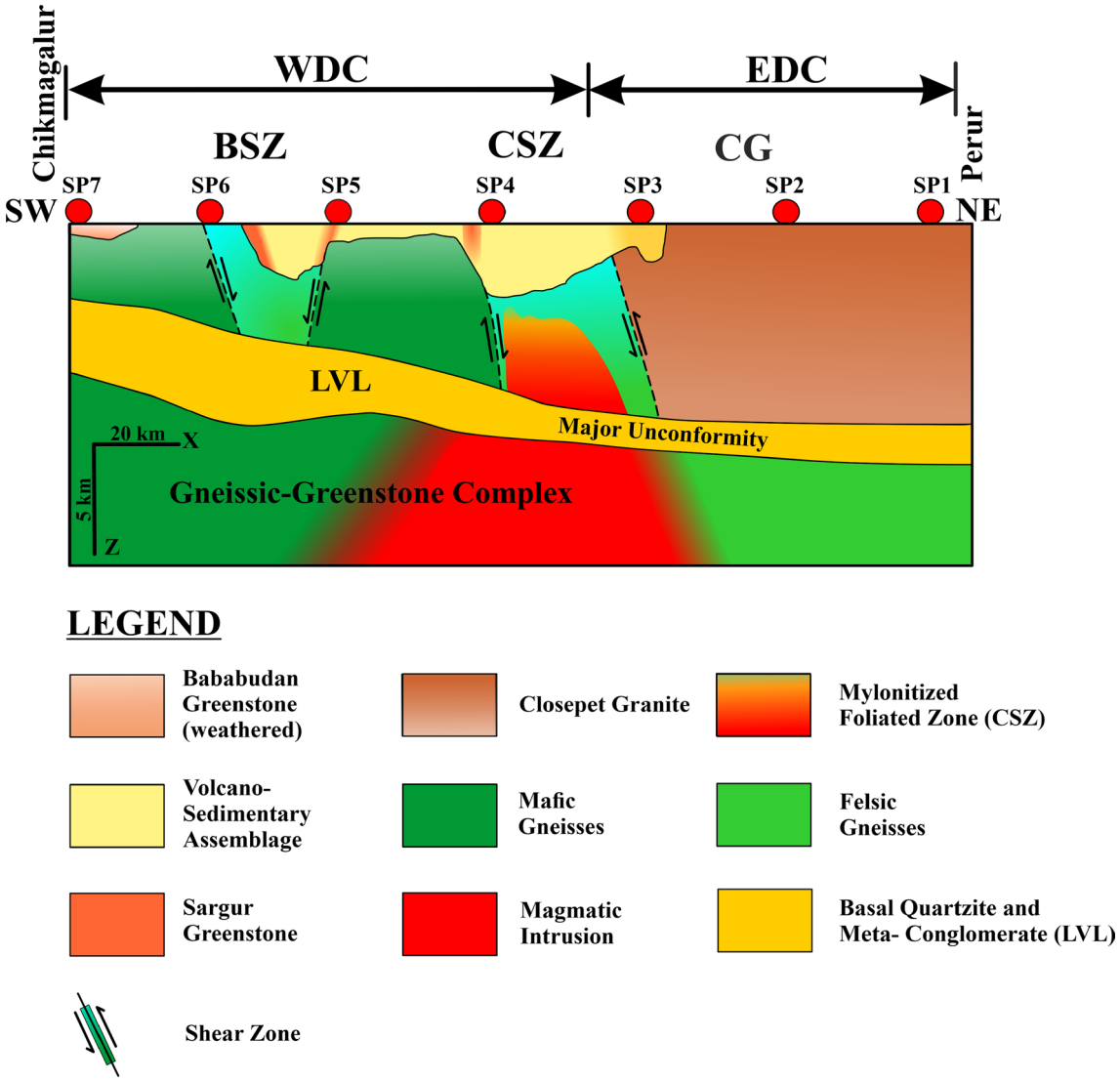

Fig. 16 Interpreted geological and tectonic model along the Perur–Chikmagalur 3-C seismic profile acquired in the Dharwar Craton of southern India. Model shows subsurface units with compositional changes of rocks in the upper crust delineated through inversion of *P*- and *S*-wave first-arrival refraction and reflection traveltime data for all the SPs (marked as red dots) acquired along the seismic profile crossing EDC and WDC parts of the craton. The major suture zone CSZ divides EDC and WDC blocks of the Dharwar Craton satisfying the presence of crocodile tectonics with exhumation of mid-to-lower crustal mafic materials because of intense shearing and transpression due to oblique convergence of two different cratonic blocks. The compositional distinction of different rock types is indicated by their respective color legend. Vertical exaggeration of the model is 4:1 for clarity

V_P/V_S (1.80) and σ (0.28) values, respectively. Hence, this zone becomes compositionally distinct with respect to adjacent EDC and WDC part of DC. On the other hand, BSZ is mainly confined within WDC having relatively low V_P (6.29 km/s), V_S (3.62 km/s), V_P/V_S (1.738) and σ (0.25) values as compared to CSZ, but clearly delineated from the V_S, V_P/V_S and σ images (Figs. 9, 10 and 11). However, these complex geological features are not deciphered from the V_P model (Fig. 7) only and not able to differentiate the geological heterogeneities or complex tectonic settings on the basis of V_P model only because of the presence of similar velocity metamorphic rocks as mentioned by Rao et al. (2015a). Therefore, the interpretation with the help of only V_P model alone may not provide all the subsurface geological features for this complex metamorphic terrain with the presence of different shear zones in the Dharwar Craton. The V_P, V_S, V_P/V_S and σ images obtained from this study using 3-C seismic data analysis also clearly depict the subsurface extension of BSZ like CSZ (Figs. 7, 9, 10 and 11), which acts as another important shear zone of WDC dividing the Chitradurga greenstone belt in NE and Bababudan greenstone belt in SW part of the seismic profile (Fig. 1a) forming

older gneisses (2.8 Ga). For better correlation and comparison with compositions of similar rocks available in analogous terrain conditions of the world (Musacchio et al. 1997; Prasad et al. 2006; Snyder et al. 2009), a suitable analysis is made for assessment of compositional changes at different depths to understand their possible linkage.

It can be inferred that the V_P/V_S ratio of rocks mainly controls the pore pressure, structure and composition (Musacchio et al. 1997). Since the upper-crustal rocks of the Dharwar Craton mainly exhibit high V_P/V_S (Fig. 10) as well as high V_P and V_S values (Figs. 7 and 9), compositional attributes are mainly assessed by suitable correlation with the Poisson's ratio (Fig. 11) computed along the 3-C seismic profile (Fig. 1a). Rocks exhibiting V_P/V_S greater than 1.75 contain important minerals like plagioclase, amphibole, pyroxene and Fe-olivine (Musacchio et al. 1997). It can be inferred that the plagioclase composition of rocks influences significantly on V_P/V_S because the increase of calcium (Ca) content in rocks correlates with rise of the V_P/V_S. But, the replacement of Fe by Mg significantly increases V_P/V_S of rocks rich in pyroxene and olivine minerals (Christensen and Mooney 1995; Christensen 1996; Musacchio et al. 1997). Therefore, it can be inferred that the maximum value of V_P/V_S (>1.75) with σ (>0.26) happens because of the abundance of mafic rocks present in the upper crust with an extension down to a maximum 15-km depth in CSZ corresponding to WDC (Figs. 10 and 11). Also, the relatively high V_P (>6.25 km/s), V_S (>3.5 km/s), V_P/V_S (>1.75) and σ (>0.25) are prominent in WDC block in contrast to EDC block (Figs. 7, 9, 10 and 11). Hence, we can infer that felsic rocks are predominant in EDC block and the corresponding rocks of WDC block are unequivocally mafic in compositions. But, their presence, especially in shear zones can be inferred as mainly mafic greenstones formed due to shearing and transpression and confined to CSZ and BSZ.

The most important factor controlling lithology of rocks is σ (Poisson's ratio). The value of σ in different rocks (Holbrook et al. 1988, 1992; White et al. 1992; Christensen 1996; Snyder et al. 2009) is commonly very sensitive to the presence of quartz ($\sigma \cong 0.08$) or mafic ($\sigma \geq 0.28$) minerals. Hence, measurements of both V_P and V_S can suitably allow computation of bulk σ for different type of rocks in the upper crust of DC. Once these results are superimposed on the similar province laboratory measurements data for different rock samples akin to the greenstone belt of Canada (Salisbury et al. 2000, 2003; Reed et al. 2005; Wang et al. 2005a, b; Snyder et al. 2009), one can easily establish the presence of igneous and sedimentary rocks mainly corresponding to mafic–ultramafic and felsic-intermediate compositions with distinct classification of the bimodal group rock assemblages (Fig. 15a). Poisson's ratio increases as composition changes to gabbro from granite and then decreases for ultramafic rocks. There is a clear distinction of different blocks based on the results of σ computed along the 3-C seismic profile of DC (Fig. 11). The top layer has alternate horsts and grabens with volcano–sedimentary assemblages having low σ (0.21–0.25) followed by felsic, mafic and ultramafic rocks with relatively large σ (0.25–0.28) in upper crust along with the presence of thin (2–4 km) LVL constrained from the traveltime data of *P*- and *S*-waves corresponding to isolated quartzite assemblage dominated by polymict meta-conglomerates with low Poisson's ratio ($\sigma = 0.23$) along the profile forming the basal unconformity (Fig. 11).

We have plotted the computed values of V_P vs V_S on the available global data set (Musacchio et al. 1997; Snyder et al. 2009) of corresponding laboratory measurements for upper-crustal rocks at 200 MPa for better understanding of the different rock compositions in the Dharwar Craton. Our results (marked as red colored dots) show (Fig. 15a) very good correlation with the different rocks (represented by colored ellipses) of the similar Archean Province of the world called Abitibi Greenstone Belt of the Canada (Snyder et al. 2009). Since the V_P vs V_S values corresponding to granites, felsic or mafic gneisses are clustered together and not resolved from this V_P vs V_S plots of the Dharwar Craton (Fig. 15a), we have tried to plot the computed values of V_P/V_S versus V_P over the only available laboratory measurements for upper-crustal rocks (200 MPa) of Grenville-Appalachian Province (North America) to observe any correlation (Musacchio et al. 1997). The Grenville–Appalachian Province is also near to the Abitibi Greenstone Province having similar structural trend with rock compositions as compared to the Dis also near to the Abitibi Greenstone Province having similar structural trend with rock compositions as compared to the Dharwar Craton of southern India. We could be able to see that there exists a distinct classification of rocks in the upper crust without any overlap and easy to distinguish based on their compositions (Fig. 15b). Similarly, we have also plotted V_P/V_S versus V_S (Fig. 15c) to show distinctions of the upper-crustal rock compositions of DC.

We have distinguished presence of three different fields from the results obtained in EDC and WDC part based on the V_P/V_S and σ (Figs. 10 and 11). The felsic field refers to rocks having more silica content, which results in less values of V_P (<6.3 km/s) and V_P/V_S (<1.75). The mafic field indicates low silica content in rocks having higher values of V_P (>6.3 km/s) and V_P/V_S (>1.75 up to 1.80). The presence of mafic field shown in Fig. 15b (top right corner) represents the mafic rocks with high plagioclase content (e.g., gabbro-norite). Based on the results of V_P/V_S versus V_P (Fig. 15b) and V_P/V_S versus V_S (Fig. 15c), obtained along the 3-C seismic profile of the Dharwar Craton, it can be inferred that there is a significant difference exist in compositions of each upper-crustal layer corresponding to the four layer model developed. This study provides a very good correlation with the compositional assemblages of Grenville-Appalachian

province and Abitibi Archean greenstone province of the North America and Canada, respectively (Musacchio et al. 1997, 2004; Snyder et al. 2009). We have also computed the elastic parameters (details of the equations used are mentioned in Appendix 2) such as the bulk modulus (K), shear modulus (μ) and Poisson's ratio (σ), which are plotted on the standard curves of Tatham (1982) to see how much deviation of our computed values of V_P/V_S and σ for the Dharwar Craton compared to the corresponding global average value of upper crust (e.g., 1.67 and 0.25) to better understand lithology and constrain composition of different rocks of the model derived in the study region (Fig. 15d).

An understanding of physical properties of different rock types with respect to the V_P/V_S—lithology association is essential for effective and suitable interpretation of the study area. Hence, a complete understanding is necessary to know how the observed variations of both V_P/V_S and σ along the present seismic profile, which are mainly controlled by variations in elastic properties of rock matrix materials. Relative variations between any two elastic constants can be related to variations of V_P/V_S. Hence, for a homogeneous and isotropic solid medium (in ideal case), only two elastic constants are necessary to describe the system. For our purposes, we will use K (bulk modulus) and μ (shear modulus), which are obtained from the V_P, V_S, V_P/V_S and σ values of the derived models (Figs. 7, 9, 10 and 11). Like the case of σ, there is a very good correlation between K/μ and V_P/V_S (Tatham 1982). For a Poisson solid, σ is 0.25, V_P/V_S is $\sqrt{3}$ (1.732), and K/μ is 5/3 (1.67). The values of V_P/V_S, σ and K/μ obtained for the 3-C seismic profile are plotted (Fig. 15d) on the standard curves (Tatham 1982). They show very good correlation of the effect of rock matrix material distribution along with the crack distribution within the mineral matrix of the whole rock samples (Fig. 15d) for suitable interpretation of observed V_P/V_S values for lithology changes of the upper-crustal rocks (Fig. 16), which helps to understand the tectonic implications of this region. This also shows a distinct classification of rocks in EDC and WDC having K/μ ranges from 1.25 to 2.2 for corresponding computed values of V_P/V_S (1.62–1.80) and σ (0.18–0.28), respectively (Figs. 10, 11 and 15d) and acts as a proxy for identification of lithology in this highly complex Archean Province of the Dharwar Craton.

Tectonic implications

An important implication of this study inferred from the results of our 3-C seismic data analysis, modeling and inversion of refraction and reflection (*P*- and *S*-waves) traveltime data is that tectonic settings of DC could be linked to continental rifting. This study also confirms the spatial extension of large batholith called Closepet Granite (Dharwar Batholith) confined in EDC and important geo-suture, namely CSZ that separates EDC and WDC blocks of DC (Newton 1990; Nutman et al. 1996; Chadwick et al. 2000; Chardon et al. 2002; Jayananda et al. 2000, 2008; Moyen et al. 2003; Meert et al. 2010; Ramakrishnan and Vaidyanadhan 2010; Manikyamba and Kerrich 2012). Based on the geological-geochemical study, four different models of geodynamic evolution were proposed for the Dharwar Craton (Naqvi and Rogers 1987; Hanson et al. 1988; Rajamani 1988; Krogstad et al. 1989; Newton 1990; Chadwick et al. 2000; Chardon et al. 2002; Jayananda et al. 2008; Sharma 2009). We can distinguish different tectonic and geological domains with the help of V_P and V_S models along with other seismic attributes like V_P/V_S, Poisson's ratio, bulk modulus and shear modulus, respectively, along the 3-C seismic profile (Fig. 1a). From this study the thickness of the greenstone belt along the profile ranges from 3.5 to 9.0 km thickening toward east (Perur) with anomalous increase of V_P (6.85 km/s), V_S (3.80 km/s), V_P/V_S (1.80) and σ (0.28) in CSZ (Figs. 7, 9, 10 and 11). The upper-crustal greenstone belt has a zone of detachment at 3–11 km depth overlain by distinct lithological and rheological properties by the presence of eastward-dipping LVL. Similar detachment zones, along with major shear zones like CSZ, are also observed in different Archean greenstone belts of Western Australia such as the Pilbara and Yilgarn cratons (Drummond et al. 1993; Wellman 2000; Van Kranendonk et al. 2004). This LVL corresponds to a major unconformity forming the detachment zone represented by basal quartz–pebble polymict meta-conglomerate, which confirms the much-debated hypothesis that the Dharwar greenstones and schists overlay on the Archean gneissic rocks sandwiched by this LVL. Toward east of CSZ, there is a N-S trending, 300 km long and ~ 40 km wide large granitic horst structure called Closepet Granite—a batholith evolved during Neoarchean collision (2.5 Ga) between EDC and WDC (Fig. 1a). This horst structure has been imaged between SP1 and SP3 in the east by low values of both V_P (6.25 km/s) and V_S (3.53 km/s) due to younger felsic granite/granulite rock compositions forming the major part of EDC as compared to its counterpart in the west with increased velocities of both V_P (6.35 km/s) and V_S (3.65 km/s) corresponding to older mafic metamorphic greenstones (schists and gneisses) of WDC. But the detachment zone prevails all along the profile having a distinct eastward dipping LVL forming a major compositional division in the upper crust (Figs. 7, 9 and 16).

Since upper-crustal structure and composition assessment are very important to comprehend the complex geology and tectonic framework of the Archean cratonic terrain, this study hitherto considers for the first time to address the geological complexity of the Archean craton of southern India. The shallow upper-crustal V_P and V_S models (Figs. 7 and 9) are derived for the 3-C seismic profile (Fig. 1a) in DC using both refraction and reflection traveltime data (Figs. 2, 3, 6 and 8).

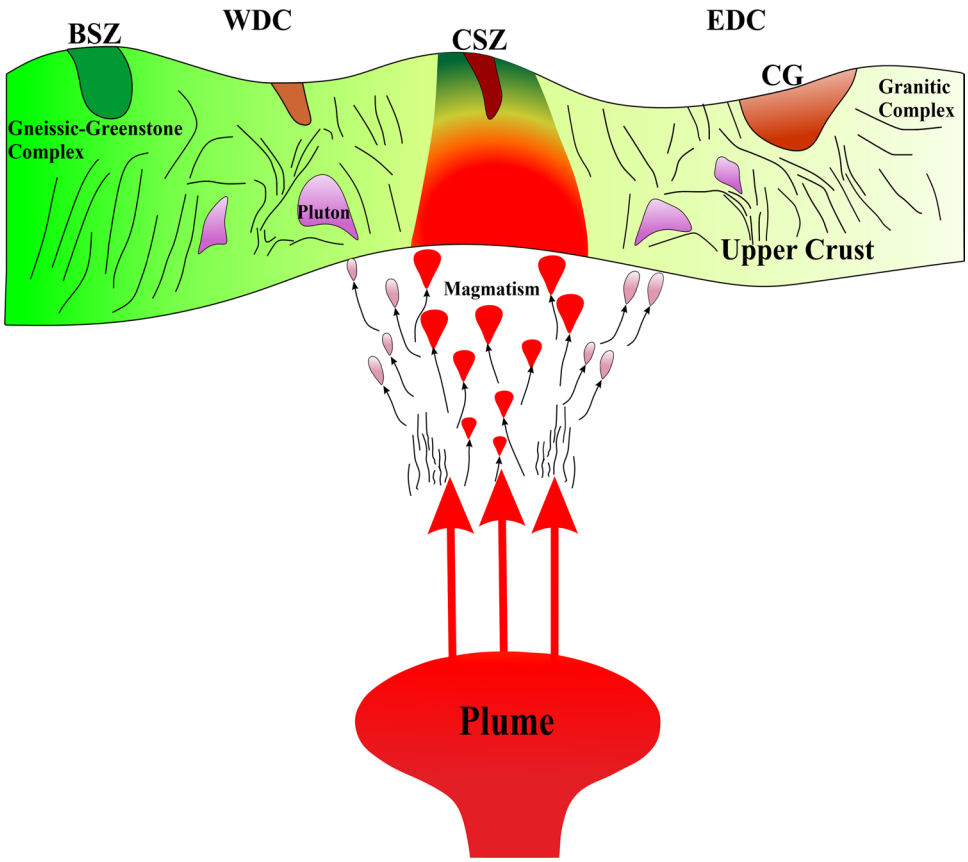

Fig. 17 Cartoon sketch representing the proposed tectonic evolution of the upper crust showing magmatic accretion due to plume activity with formation of major suture zone (CSZ) dividing Mesoarchean mafic gneissic-greenstone complex (WDC) and Neoarchean felsic granitic complex (EDC) of the Dharwar Craton

This helps to build the geologically reasonable comprehensive tectonic model (Fig. 16) for suitable interpretation of both subsurface geological structures as well as lithological/compositional variations of diverse rock types in this region along the profile. The important subsurface geological features imaged are (1) presence of horst and grabens all along the profile representing granites, gneisses and greenstones in EDC and WDC blocks, (2) important shear zones, (3) spatial extension of deepseated compositional anomaly for CSZ separating EDC and WDC, (4) exposures of high-velocity mafic materials of mid-to-lower crust because of large-scale volcanism and magmatism (~ 1 Ga) and (5) presence of east dipping LVL as a zone of detachment squeezed between the Dharwar schists and Archean gneisses. All these subsurface geological attributes when integrated provide necessary information on the presence of major suture formed along CSZ. This led to oblique convergence along with shortening of EDC and WDC blocks represented by large thrust and the zone of accretion with magmatism due to deepseated plume activity shown as a sketch indicating the tectonic evolution of this region (Fig. 17). The results obtained further vindicate the plume-arc model of evolution with contemporaneous felsic volcanism toward EDC and sub-contemporaneous mafic volcanism in WDC with the formation of greenstone-TTG basement. The zone of accretion is mainly represented by crustal growth followed by detachment processes leading to sandwich of firm rigid layers with the weak zones (LVL) to produce crocodile structure (Meissner 1989) as observed in our study along the profile forming a large suture (CSZ) in DC cutting across EDC and WDC blocks. Hence, WDC block represents multiphase tectonics with a major suture zone CSZ forming a distinct compositional boundary (Figs. 16 and 17). This also supports the cryptic suture model of Naqvi (1985) represented by the large shear zone between EDC and WDC having volcano–sedimentary facies assemblages of CSZ. This might have been formed due to the basin closure located between these two continental blocks (EDC and WDC) forming a tectonic wedge (Fig. 16) with some form of accretion and collision tectonics prevalent in the Dharwar Craton (Fig. 17).

Conclusions

This study presents V_P and V_S modeling of DC along with compositional assessments of different rocks. The important conclusions of this study are as follows:

(1) Both *P*-wave (V_P=5.4–6.9 km/s) and *S*-wave (V_S=3.24–3.98 km/s) velocity models show four-layered upper-crustal structures with the presence of very shallow horst and grabens having volcanic sedimentary assem-

blages, felsic and mafic granite–gneiss–greenstones, low-velocity-layer (LVL) as a zone of detachment with polymict meta-conglomerates, the presence of numerous faults and shear zones to decipher CSZ and BSZ as well as large-scale granitic plutons/batholiths of Closepet Granite.

(2) The CSZ with anomalous increase of V_P (6.85 km/s), V_S (3.80 km/s), V_P/V_S (1.80) and σ (0.28) acts as a major suture zone where mid-to-lower crustal mafic materials (i.e., greenstones) deposited at shallow depth because of oblique convergence and intense shearing of two different cratonic blocks of DC.

(3) A clear distinction of compositional changes of two major blocks revealed from the V_P/V_S and σ estimates represents EDC block as mainly felsic- and quartz-rich younger granites as compared to WDC dominated by greenschists, amphibolites, gneisses, granulite–facies mafic and ultramafic rocks.

(4) The integrated interpretation of V_P, V_S, V_P/V_S and σ deciphers the upper-crustal structure and compositions in the Dharwar Craton to propose a robust tectonic model for the study region.

(5) The variation of σ (0.20–0.28) for different crustal rock types provides important information on the lithology and rock compositions, showing older mafic rocks dominant in WDC part as compared to younger felsic rocks in EDC.

(6) The LVL acts as a major zone of detachment forming a prominent unconformity over which the Dharwar schist belts rest on the Archean gneisses.

(7) The computed values of K/μ (1.25–2.2), V_P/V_S (1.62–1.80) and σ (0.18–0.28) correlate very well with the standard curves of Tatham (1982), which acts as a proxy for identification of different lithology and rock compositions in this study region.

(8) The geologically plausible tectonic model derived in this Archean Province of the Dharwar Craton is well constrained from V_P, V_S, V_P/V_S and σ variations along the profile to help mineral prospect of this study region.

(9) The evidence of plume-arc evolutionary model is inferred for the Dharwar Craton supported by both felsic and mafic magmatism corroborated by deepseated plume–craton interactions.

Appendix 1: Field statics corrections

In order to remove the effect of near-surface weathering and elevations along the seismic profile, field statics (shot statics, receiver statics and datum statics) corrections are applied to the seismic data. This can be illustrated with the help of the schematic sketch shown below. If shots (denoted by *S*) are located below the weathering layer (as in our case of land seismic data acquisition and the explosives are put in shot holes drilled along the seismic profile shown in Fig. 1), then the total datum static correction to apply to the trace associated with midpoint *M* is $t_D = -(t_S + t_R)$, where t_S and t_R are the shot and receiver static corrections down to a specified datum *D*. It is a known convention that static correction is negative if both sources and receivers are above the datum and positive if they are below the datum. From the geometry of the sketch shown below, $t_S = \frac{E_S - E_D - D_S}{v_b}$ and $t_R = \frac{E_R - E_D - D_R}{v_b}$. Hence, the field statics corrections with reference to the datum $\Delta\tau_D$ can be computed as (Yilmaz 2001):

$$\Delta\tau_D = -\frac{E_S - E_D - D_S}{v_b} - \frac{E_R - E_D - D_R}{v_b} - t_{UH}, \quad (1)$$

$$\Delta\tau_D = \frac{2E_D - (E_S - D_S) - (E_R - D_R)}{v_b} - t_{UH}, \quad (2)$$

where E_D is the datum elevation, E_S and E_R are the surface elevations at the shot and receiver stations, D_S is the depth of the shot hole beneath the shot stations, D_R is the depth of the shot hole near the receiver station, t_{UH} is the uphole time measured at the receiver location (the time associated with the distance D_R as shown in the schematic sketch below. The shot, receiver and datum elevations along with depth of each shot hole are measured during topographical survey and shot hole drilling along the seismic profile before seismic data recording and blasting of each shot hole. The sub-weathering velocity v_b corresponds to the bedrock velocity, which is obtained from the deep uphole survey conducted in the study area while seismic field operations. An uphole survey involves placing shots down the hole at various depth levels (which is drilled so that maximum depth reaches below the weathering layer), then recording the arrivals at the surface near the hole. The plot of time versus depth provides the bedrock velocity of the study region (Yilmaz 2001).

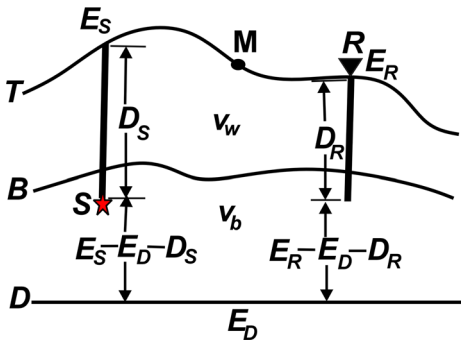

Appendix 2: Estimation of compositional attributes

The formulas used for the computation of compositional attributes such as bulk modulus (K) and shear modulus (μ) are mentioned below. From the seismic data analysis, we have obtained V_P and V_s of different rocks in the Dharwar Craton (Fig. 1). To compute K for the different rocks in this region, we require the Lame's parameter λ, μ and the density (ρ) of the different rocks. We have computed density values (ρ) along the seismic profile at different velocity nodes of V_P (Fig. 7) using the Nafe and Drake (1957) and Ludwig et al. (1970) empirical formula for the upper-crustal rocks of this hard rock terrain of the Dharwar Craton. The shear modulus μ along the profile is computed as (Telford et al. 1988):

$$\mu = \rho V_S^2. \tag{3}$$

Then the computation of Lame's parameter λ is made along the profile using V_P, V_S and μ as (Salisbury et al. 2003):

$$\lambda = \rho V_P^2 - 2\mu. \tag{4}$$

The corresponding bulk modulus K can be obtained at each node of the V_P and V_S models (inset of Figs. 15a) derived for the Dharwar Craton using the following equation as (Telford et al. 1988):

$$\mathrm{K} = \lambda + \frac{2}{3}\mu. \tag{5}$$

Supplementary Information The online version contains supplementary material available at https://doi.org/10.1007/s11600-023-01226-x.

Acknowledgements We sincerely thank Dr. V. M. Tiwari, Director, CSIR-NGRI, to accord permission for publication of this paper. We sincerely thank Prof. Colin A. Zelt of Rice University, USA, for using his RAYINVR software codes and ProMAX software of Halliburton Pty., USA, in this data analysis. DK sincerely thanks Department of Science and Technology (DST, Govt. of India) for award of DST-INSPIRE Fellowship to pursue his PhD under this project in CSIR-NGRI. The CSS Group of CSIR-NGRI is duly acknowledged for 3-C seismic data acquisition in the Dharwar field operations. The work corresponds to the scientific contributions of the project MLP-6402-28 (LB) of CSIR-NGRI.

Declarations

Conflict of interest On behalf of all authors, the corresponding author states that there is no conflict of interest.

References

Arndt NT (2003) Komatiites, Kimberlites and boninites. J Geophys Res 108(B6):5–11. https://doi.org/10.1029/2002JB002157

Arndt NT, Kerr AC, Tarney J (1997) Dynamic melting in plume heads: the formation of Gorgana komatiites and basalts. Earth Planet Sci Letts 146:289–301

Behera L (2011a) Seismic imaging of Mahanadi delta and its tectonic significance. Lap Lambert Academic Publishing GmbH and Co KG, Germany, p 146

Behera L (2011b) Crustal tomographic imaging and geodynamic implications toward south of Southern Granulite Terrain (SGT), India. Earth Planet Sci Letts 309(1–2):166–178. https://doi.org/10.1016/j.epsl.2011.04.033

Behera L, Kumar D (2022) Deep crustal structure and compositions for tectonic and geodynamic implications of the Dharwar Craton (Southern India) inferred from 3-C wide-angle seismic data. J Asian Earth Sci 227(105092):1–37. https://doi.org/10.1016/j.jseaes.2022.105092

Behera L, Sarkar D (2011) Tomographic imaging of large volcanic province due to intense magmatism in the Mahanadi delta of eastern India. Physics Earth Planet Int 189(3–4):142–150. https://doi.org/10.1016/j.pepi.2011.08.005

Behera L, Sen MK (2014) Tomographic imaging of sub-basalt Mesozoic sediments and shallow basement geometry for hydrocarbon potential below the Deccan Volcanic Province (DVP) of India. Geophys J Int 199:296–314. https://doi.org/10.1093/gji/ggu261

Behera L, Sain K, Reddy PR, Rao IBP, Sarma VYN (2002) Delineation of shallow structure and the Gondwana graben in the Mahanadi delta, India, using forward modeling of first arrival seismic data. J Geodyn 34:127–139

Behera L, Sain K, Reddy PR (2004) Evidence of underplating from seismic and gravity studies in the Mahanadi delta of eastern India and its tectonic significance. J Geophys Res 109(B12311):1–25. https://doi.org/10.1029/2003JB002764

Behera L, Kolluru R, Singh B (2021) Imaging Mesozoic sediments in Deccan Volcanic province of India: inferences from seismic and gravity studies. J Geol Soc Ind 97:1260–1273. https://doi.org/10.1007/s12594-021-1855-3

Bhaskar Rao YJ, Vijay Kumar T, Krishna KVSS, Thomson JK (2008) The emerging pattern of crust-formation and recycling history in the Precambrian Dharwar Craton and Southern Granulite Terrain, southern India, constraints from recent geochronological and isotopic results. J Geol Soc Ind 74:147–168

Červený V, Molotkov I, Pšenčík I (1977) Ray method in seismology. University of Karlov Press, Prague, Czechoslovakia

Chadwick B, Vasudev VN, Hegde GV (1997) The Dharwar Craton, southern India, and its Late Archaean plate tectonic setting: current interpretations and controversies. Indian Acad Sci (Earth Planet Sci) Proceed 106(4):1–10

Chadwick B, Vasudev VN, Hegde GV (2000) The Dharwar Craton, southern India, interpreted as the result of Late Archean oblique convergence. Precambrian Res 99:91–101

Chadwick B, Vasudev VN, Hegde GV, Nutman AP (2007) Structure and SHRIMP U/Pb zircon ages of granites adjacent to the Chitradurga schist belt: implications for Neoarchean convergence in the Dharwar Craton, Southern India. J Geol Soc Ind 69:5–24

Chardon D, Choukroune P, Jayananda M (1996) Strain patterns, decollement and incipient sagducted greenstone terrains in the Archean Dharwar Craton (South India). J Struct Geol 19:991–1004

Chardon D, Choukroune P, Jayananda M (1998) Sinking of the Dharwar basin (South India): implications for Archean tectonics. Precam Res 91:15–39

Chardon D, Peucat J-J, Jayananda M, Choukroune P, Fanning CM (2002) Archean granite-greenstone tectonics at Kolar (South India): interplay of diapirism and bulk inhomogeneous contraction during juvenile magmatic accretion. Tectonics 21(3):1–17. https://doi.org/10.1029/2001TC901032

Chardon D, Jayananda M, Chetty TRK, Peucat J-J (2008) Precambrian continental strain and shear zone patterns: South Indian case. J Geophys Res 113(B08402):1–16. https://doi.org/10.1029/2007JB005299

Chardon D, Jayananda M, Peucat J-J (2011) Lateral constructional flow of hot orogenic crust: insights from the Neoarchean of south India, geological and geophysical implications for orogenic plateau. Geochem Geophys Geosyst 12:1–24. https://doi.org/10.1029/2010GC003398

Choukroune P, Ludden JN, Chardon D, Calvert AJ, Bouhallier H (1997) Archean crustal growth and tectonic processes: a comparison of Superior Province, Canada, and the Dharwar Craton. Indian Geol Soc Spl Publ 121:63–98

Christensen NI (1996) Poisson's ratio and crustal seismology. J Geophys Res 101(B2):3139–3156

Christensen NI, Mooney WD (1995) Seismic velocity structure and composition of the continental crust: a global review. J Geophys Res 100(B6):9761–9788. https://doi.org/10.1029/95JB00259

Condie KC (1994) Archean crustal evolution. Developments in Precambrian geology 11. Elsevier, Amsterdam, The Netherlands, p 528

Devaraju TC, Viljoen RP, Sawkar RH, Sudhakara TL (2009) Mafic and ultramafic magmatism and associated mineralization in the Dharwar Craton, Southern India. J Geol Soc Ind 73:73–100

Dey S (2013) Evolution of Archean crust in the Dharwar Craton: the Nd isotope record. Precambrian Res 227:227–246. https://doi.org/10.1016/j.precamres.2012.05.005

Drummond BJ, Goleby BR, Swager CP, Williams PR (1993) Constraints on Archean crustal composition and structure provided by deep seismic sounding in the Yilgarn Block. Ore Geol Rev 8:117–124

Fernandez-Viejo G, Clowes RM, Welford JK (2005) Constraints on the composition of the crust and uppermost mantle in northwestern Canada: V_P/V_S variations along Lithoprobe's SNorCLE transect. Can J Earth Sci 42:1205–1222. https://doi.org/10.1139/E05-028

Firbas P (1987) Tomography from seismic profiles. In: Nolet G, Dordrecht R (eds) Seismic Tomography, pp 189–202

Franco RD (2011) Refractor velocity analysis: a signal processing procedure. Geophys Prosp 59:432–454. https://doi.org/10.1111/j.1365-2478.2010.00931.x

Gajewski D, Prodhel C (1987) Seismic refraction investigation of the Black Forest. Tectonophysics 142:27–48

GSI ISRO (1994) Project Vasundhara: Generalized geological map (scale 1:2 million). Geol Surv Ind, Ind Space Res Org, Bangalore

Guevara SE, Stewart R (1998) Multicomponent seismic polarization analysis. CREWES Res Rep 10:7–19

Hanson GN, Krogstad EJ, Rajamani V (1988) Tectonic setting of the Kolar Schist Belt, Karnataka, India (Abstract). Workshop on The Deep Cont Crust of South Ind Jan 1988, Field Excursion Guide, pp 40–42

Harish Kumar SB, Jayananda M, Kano T, Shadakshara Swamy N, Mahabaleswar B (2003) Late Archean juvenile magmatic accretion process in the Eastern Dharwar Craton: Kuppam-Karimangalam Area. Geol Soc Ind Mem 50:375–408

Holbrook WS, Gajewski D, Krammer A, Prodehl C (1988) An interpretation of wide angle compressional and shear-wave data in southwest Germany: Poisson's ratios and petrological implications. J Geophys Res 93(B10):12081–12106

Holbrook WS, Mooney WD, Christensen NI (1992) The seismic velocity of the deep continental crust. In: Fountain DM, Arculus R, Kay RW (eds) Continental lower crust. Elsevier, NY, pp 1–34

Huang H, Spencer C, Green A (1986) A method for the inversion of refraction and reflection travel times for laterally varying velocity structures. Bull Seismol Soc Am 76:837–846

Iannaccone G, Improta L, Capuano P, Zollo A, Biella G, Franco RD, Deschamps A, Massimo C, Mirabile L, Romeo R (1998) A P-wave velocity model of the upper crust of the Sannio region (Southern Apennines, Italy). Ann Geofis 41(4):567–582

Jayananda M, Moyen J-F, Martin H, Peucat J-J, Auvray B, Mahabaleshwar B (2000) Late Archean (2550–2520 Ma) juvenile magmatism in the eastern Dharwar Craton, southern India: constraints from geochronology, Nd-Sr isotopes and whole rock geochemistry. Precam Res 99:225–254

Jayananda M, Chardon D, Peucat J-J, Capdevila R (2006) 2.61 Ga potassic granites and crustal reworking in the western Dharwar Craton, southern India: tectonic, geochronologic and geochemical constraints. Precam Res 150:1–26. https://doi.org/10.1016/j.precamres.2006.05.004

Jayananda M, Kano T, Peucat J-J, Channabasappa S (2008) 3.35 Ga komatiite volcanism in the western Dharwar Craton, southern India: constraints from Nd isotopes and whole rock geochemistry. Precam Res 162(1–2):160–179. https://doi.org/10.1016/j.precamres.2007.07.010

Jayananda M, Peucat J-J, Chardon D, Krishna Rao B, Fanning CM, Corfu F (2013a) Neoarchean greenstone volcanism and continental growth, Dharwar Craton, southern India: constraints from SIMS U-Pb zircon geochronology and Nd isotopes. Precam Res 227:55–76. https://doi.org/10.1016/j.precamres.2012.05.002

Jayananda M, Tsutsumi Y, Miyazaki T, Gireesh RV, Kapfo K, Tushipokla HH, Kano T (2013b) Geochronological constraints on Meso- and Neoarchean regional metamorphism and magmatism in the Dharwar Craton, southern India. J Asian Earth Sci 78:18–38. https://doi.org/10.1016/j.jseaes.2013.04.033

Jayananda M, Gireesh RV, Sekhamo KU, Miyazaki T (2014) Coeval felsic and mafic magma in Neoarchean calc-alkaline magmatic arcs, Dharwar Craton, southern India: field and petrographic evidence from mafic to hybrid magmatic enclaves and synplutonic mafic dykes. J Geol Soc Ind 84:5–28

Johnston JE, Christensen NI (1993) Compressional to shear velocity ratios in sedimentary rocks. Int J Rock Mech Min Sci Geomech Abstr 30(7):751–754. https://doi.org/10.1016/0148-9062(93)90018-9

Kaila KL, Chowdhury KR, Reddy PR, Krishna VG, Narain H, Subbotin SI, Sollogub Chekunov AV, Kharetchko LMA, Ilchenko TC (1979) Crustal structure along Kavali-Udipi profile in the Indian peninsular shield from deep seismic sounding. J Geol Soc Ind 20:307–333

Kerr AC, Marriner GF, Arndt NT, Tarney J, Nivia A, Saunders AD, Duncan R (1996) The petrogenesis of Gorgona komatiites, picrites and basalts: new field, petrographic and geochemical constraints. Lithos 37:245–260

Kerrich R, Xie Q (2002) Compositional recycling structure of an Archean super-plume: Nb-Th-U-LREE systematics of Archean Komatiites and basalts revisited. Contrib Min Petrol 142:476–484

Krogstad EJ, Balkrishnan S, Hanson G, Rajamani V (1989) Plate tectonics at 2.5 Ga ago: evidence from Kolar Schist Belt, South India. Science 243:1337–1340

Kumar A, Nagaraju E, Besse J, Bhaskar Rao YJ (2012) New age, geochemical and paleomagnetic data on a 2.21 Ga dyke swarm from south India: constraints on Paleoproterozoic reconstruction. Precam Res 220–221:123–138. https://doi.org/10.1016/j.precamres.2012.08.001

Ludwig WJ, Nafe JE, Drake CL (1970) Seismic refraction, New concepts of sea floor evolution. In: Maxwell AE (eds), The Sea. Wiley-Interscience, Hoboken, NJ vol 4(1), pp 53–84

Lutter WJ, Nowack RL, Braile LW (1990) Seismic imaging of upper crustal structure using travel times from the PASSCAL Ouachita experiment. J Geophys Res 95:4621–4631

Malinowski M, Żelaźniewicz A, Grad M, Guterch A, Janik T, CELEBRATION Working Group (2005) Seismic and geological

structure of the crust in the transition Baltica to Palaeozoic Europe in SE Poland—CELEBRATON 2000 experiment, profile CEL02. Tectonophysics 401:55–77

Manikyamba C, Kerrich R (2012) Eastern Dharwar Craton, India: continental lithosphere growth by accretion of diverse plume and arc terranes. Geosci Front 3(3):225–240. https://doi.org/10.1016/j.gsf.2011.11.009

Manikyamba C, Kerrich R, Naqvi SM, Ram Mohan M (2004) Geochemical systematics of tholeiitic basalts from the 2.7 Ga Ramagiri-Hungund composite greenstone belt. Dharwar Craton Precam Res 139:21–39

Manikyamba C, Ganguli S, Saha A, Santosh M, Singh MR, Subba Rao DV (2014) Continental lithospheric evolution: constraints from the geochemistry of felsic volcanic rocks in the Dharwar Craton, India. J Asian Earth Sci 95:65–80. https://doi.org/10.1016/j.jseaes.2014.05.015

Meert JG, Pandit MK, Pradhan VR, Banks J, Sirianni R, Stroud M, Newstead B, Gifford J (2010) Precambrian crustal evolution of Peninsular India: A3.0 billion year odyssey. J Asian Earth Sci 39:483–515. https://doi.org/10.1016/j.jseas.2010.04.026

Meissner R (1989) Rupture, creep, lamellae and crocodiles: happenings in the continental crust. Terra Nova 1:17–28. https://doi.org/10.1111/j.1365-3121.1989.tb00321.x

Moyen J-F, Martin H, Jayananda M, Auvray B (2003) Late Archean granites: a typology based on the Dharwar Craton (India). Precam Res 127:103–123. https://doi.org/10.1016/S0301-9268(03)00183-9

Musacchio G, Mooney WD, Luetgert JH, Christensen NI (1997) Composition of the crust in the Grenville and Appalachian Provinces of North America inferred from V_P/V_Sratios. J Geophys Res 102(B7):15225–15241

Musacchio G, White DJ, Asudeh I, Thomson CJ (2004) Lithospheric structure and composition of the Archean western Superior Province from seismic refraction/wide-angle reflection and gravity modeling. J Geophys Res 109(B03304):1–28. https://doi.org/10.1029/2003JB002427

Nafe JE, Drake CL (1957) Variation with depth in shallow and deep water marine sediments of porosity, density and the velocities of compressional and shear waves. Geophysics 22:523–552

Naqvi SM (1985) Chitradurga schist belt—an Archean suture (?). J Geol Soc Ind 26:511–525

Naqvi SM, Rogers JJW (1987) Precambrian geology of India. In: Oxford monographs on geology and geophysics, Oxford University Press, Oxford

Newton RC (1990) The late Archean high-grade terrain of South India and deep structure of the Dharwar Craton. In: Salisbury MH, Fountain DM (eds) Exposed cross-sections of the continental crust. Kluwer, The Netherlands, pp 305–326

Nutman AP, Chadwick B, Krishna Rao B, Vasudev VN (1996) SHRIMP U/Pb zircon ages of acid volcanic rocks in the Chitradurga and Sandur groups, and granites adjacent to the Sandur schist belt, Karnataka. J Geol Soc Ind 47:153–164

Ohtani E, Kawabe I, Moriyama J, Nagata Y (1989) Partitioning of elements between majorite garnet and melt and implications for petrogenesis of komatiites. Contrib Mineral Petrol 103:263–269

Pandey OP, Chandrakala K, Vasanthi A, Satish Kumar K (2018) Seismically imaged shallow and deep crustal structure and potential field anomalies across the Eastern Dharwar Craton, south Indian shield: possible geodynamical implications. J Asian Earth Sci 157:302–316. https://doi.org/10.1016/j.jseaes.2017.11.026

Parman SW, Dann JC, Grove TL, deWit MJ (1997) Emplacement conditions of komatiite magmas from the 3.49 Ga Komati Formation, Barberton greenstone belt, South Africa. Earth Planet Sci Letts 150:303–323

Parman SW, Grove TL, Dann JC (2001) The production of Barberton komatiites in an Archean subduction zone. Geophys Res Letts 28:2513–2516

Polat A, Kerrich R (2000) Archean greenstone belt magmatism and the continental growth-mantle evolution connection: constraints from Th-U-Nb-LREE systematics of the 2.7 Ga Wawa subprovince, Superior province, Canada. Earth Planet Sci Letts 175:41–54

Prasad BR, Behera L, Rao PK (2006) A tomographic image of upper crustal structure using P and S wave seismic refraction data in the southern granulite terrain (SGT), India. Geophys Res Letts 33(L14301):1–5. https://doi.org/10.1029/2006GL026307

Puchtel IS, Hofmann AW, Amelin YV, Garbe-Schonberg CD, Samsonov AV, Shchipansky AA (1999) Combined mantle plume-island arc model for the formation of the 2.9 Ga Sumo-zero-Kenozero greenstone belt, SE Baltic shield: isotope and trace element constraints. Geochim Cosmochim Acta 63:3579–3595

Radhakrishna BP, Naqvi SM (1986) Precambrian continental crust of India and its evolution. J Geol 94:145–166

Rai SS, Priestley K, Suryaprakasam K, Srinagesh D, Gaur VK, Du Z (2003) Crustal shear velocity structure of the south Indian shield. J Geophys Res 108(B2):1–12. https://doi.org/10.1029/2002JB001776

Rajamani V (1988) The Kolar Schist Belt (Abstract). Workshop on The Deep Continental Crust of South India. Field Excursion Guide, pp 24–36

Ramakrishnan M, Vaidyanadhan R (2010) Geology of India, 2nd ed. Geol Soc Ind 1, Bangalore, p 994

Ram Mohan M, Piercey SJ, Kamber BS, Srinivasa Sarma D (2013) Subduction related tectonic evolution of the Neoarchean eastern Dharwar Craton, southern India: new geochemical and isotopic constraints. Precam Res 227:204–226. https://doi.org/10.1016/j.precamres.2012.06.012

Rao VV, Daomdar N, Sain K, Sen MK, Murty ASN, Sarkar D (2015a) Upper crust of the Archean Dharwar craton in southern India as revealed by seismic refraction tomography and its geotectonic implications. Geophys J Int 200:652–663. https://doi.org/10.1093/gji/ggu425

Rao VV, Murty ASN, Sarkar D, Bhaskar Rao YJ, Khare P, Prasad ASSSRS, Sridher V, Raju S, Rao GSP, Karuppannan, Prem Kumar N, Sen MK (2015b) Crustal velocity structure of the Neoarchean convergence zone between the eastern and western blocks of Dharwar Craton, India from seismic wide-angle studies. Precam Res 266:282–295. https://doi.org/10.1016/j.precamres.2015.05.006

Reddy PR, Chandrakala K, Sridhar AR (2000) Crustal velocity structure of the Dharwar Craton, India. J Geol Soc Ind 55:381–386

Reed LE, Snyder DB, Salisbury M (2005) 2D reflection seismic surveying in the Timmins/Kirkland lake area, Northern Ontario, Canada; acquisition, processing, interpretation: Discover Abitibi Initiative. Ontario Geol Surv Open File Rep 6169

Rumpfhuber E-M, Keller GR (2009) An integrated analysis of controlled and passive source seismic data across an Archean-Proterozoic suture zone in the Rocky Mountains. J Geophys Res 114(B08305):1–25. https://doi.org/10.1029/2008JB005886

Sain K, Kaila KL (1994) Inversion of wide-angle seismic reflection times with damped least-squares. Geophysics 59:1735–1744

Salisbury MH, Milkereit B, Ascough G, Adair R, Mathews L, Schmitt DR, Mwenifumbo J, Eaton DW, Wu J (2000) Physical properties and seismic imaging of massive sulfides. Geophysics 65:1882–1889

Salisbury MH, Harvey CW, Mathews L (2003) The acoustic properties of ores and host rocks in hardrock terranes. In: Eaton DW, Milkereit B, Salisbury MH (eds), Hardrock Seismic Exploration. Society of Exploration Geophysicists, Geophysical Development Series vol 10, pp 9–19

Sarkar D, Chandrakala K, Padmavathi Devi P, Sridhar AR, Sain K, Reddy PR (2001) Crustal velocity structure of western Dharwar Craton, south India. J Geodyn 31:227–241

Sarkar D, Ravi Kumar M, Saul J, Kind R, Raju PS, Chadha RK, Shukla AK (2003) A receiver function perspective of the Dharwar Craton (India) crustal structure. Geophys J Int 154:205–211

Sharma RS (2009) Cratons of the Indian shield. In: Cratons and fold belts of India. Lecture Notes in Earth Sciences 127, Springer, Berlin, Heidelberg, pp 41–115. https://doi.org/10.1007/978-3-642-01459-8_2

Snyder DB, Cary P, Salisbury M (2009) 2D–3C high-resolution seismic data from Abitibi Greenstone Belt, Canada. Tectonophysics 472:226–237. https://doi.org/10.1016/j.tecto.2008.05.038

Spence GD (1984) Seismic structure across the active subduction zone of western Canada. PhD Thesis, University of British Columbia

Spence GD, Clowes RM, Ellis RM (1985) Seismic structure across the active subduction zone of western Canada. J Geophys Res 90:6754–6772

Swami Nath J, Ramakrishnan M (1981) The early Precambrian supracrustals of southern Karnataka. Mem Geol Soc Ind 112:1–350

Talukdar K, Behera L (2018) Sub-basalt imaging of hydrocarbon-bearing Mesozoic sediments using ray-trace inversion of first-arrival seismic data and elastic finite-difference full-wave modeling along Sinor-Valod profile of Deccan Syneclise, India. Pure Appl Geophys 175(8):2931–2954. https://doi.org/10.1007/s00024-018-1831-z

Tarantola A (1987) Inverse problem theory. Elsevier, Amsterdam

Tatham RH (1982) V_P/V_S and lithology. Geophysics 47(3):336–344

Telford WM, Geldart LP, Sheriff RE, Keys DA (1988) Applied Geophysics. Cambridge University Press, Oxford and IBH Publishing Co Pvt Ltd, New Delhi

Van Kranendonk MJ, Collins WJ, Hickman A, Pawley MJ (2004) Critical tests of vertical vs. horizontal tectonic models for the Archean east Pilbara granite-greenstone terrane, Pilbara Craton, western Australia. Precam Res 131:173–211. https://doi.org/10.1016/j.precamres.2003.12.015

Wang Q, Ji S, Salisbury MH, Xia B, Pan M, Xu Z (2005a) Pressure dependence and anisotropy of P-wave velocities in ultrahigh-pressure metamorphic rocks from the Dabie-Sulu orogenic belt (China): implications for seismic properties of subducted slabs and origin of mantle reflections. Tectonophysics 398:67–99. https://doi.org/10.1016/j.tecto.2004.12.001

Wang Q, Ji S, Salisbury MH, Xia B, Pan M, Xu Z (2005b) Shear wave properties and Poisson's ratios of ultrahigh-pressure metamorphic rocks from the Dabie-Sulu orogenic belt, China: implications for crustal compositions. J Geophys Res 110(B08208):1–28. https://doi.org/10.1029/2004JB003435

Wellman P (2000) Upper crust of the Pilbara Craton, Australia: 3D geometry of granite/greenstone terrain. Precam Res 104:175–186

White DJ, Milkereit B, Salisbury MH, Percival JA (1992) Crystalline lithology across the Kapuskasing uplift determined using in situ Poisson's ratio from seismic tomography. J Geophys Res 97(B13):19993–20006

Yilmaz Ö (2001) Seismic data analysis. Society of Exploration Geophysicists, Tulsa, OK

Zandt G, Ammon CJ (1995) Continental crust composition constrained by measurements of crustal Poisson's ratio. Nature 374(6518):152–154

Zelt CA (1999) Modeling strategies and modeling assessment for wide-angle seismic traveltime data. Geophys J Int 139:183–204. https://doi.org/10.1046/j.1365-246X.1999.00934.x

Zelt CA, Ellis RM (1988) Practical and efficient ray tracing in two-dimensional media for rapid traveltime and amplitude forward modeling. Can J Explor Geophys 24:16–31

Zelt CA, Smith RB (1992) Seismic traveltime inversion for 2-D crustal velocity structure. Geophys J Int 108:16–34. https://doi.org/10.1111/j.1365-246X.1992.tb00836.x